# Beyond Binary Classification: A Semi-supervised Approach to Generalized AI-generated Image Detection

## Hong-Hanh Nguyen-Le<sup>1</sup>, Van-Tuan Tran<sup>2</sup>, Dinh-Thuc Nguyen<sup>3</sup>, Nhien-An Le-Khac<sup>1</sup>

<sup>1</sup> School of Computer Science, University College Dublin, Ireland
<sup>2</sup> School of Computer Science and Statistics, Trinity College Dublin, Ireland
<sup>3</sup> Department of Knowledge Engineering, University of Science, VNU-HCMC, Vietnam hong-hanh.nguyen-le@ucdconnect.ie, tranva@tcd.ie, ndthuc@fit.hcmus.edu.vn, an.lekhac@ucd.ie

#### Abstract

The rapid advancement of generators (e.g., StyleGAN, Midjourney, DALL-E) has produced highly realistic synthetic images, posing significant challenges to digital media authenticity. These generators are typically based on a few core architectural families, primarily Generative Adversarial Networks (GANs) and Diffusion Models (DMs). A critical vulnerability in current forensics is the failure of detectors to achieve cross-generator generalization, especially when crossing architectural boundaries (e.g., from GANs to DMs). We hypothesize that this gap stems from fundamental differences in the artifacts produced by these distinct architectures. In this work, we provide a theoretical analysis explaining how the distinct optimization objectives of the GAN and DM architectures lead to different manifold coverage behaviors. We demonstrate that GANs permit partial coverage, often leading to boundary artifacts, while DMs enforce complete coverage, resulting in over-smoothing patterns. Motivated by this analysis, we propose the **Tri**archy **Detect**or (TriDetect), a semi-supervised approach that enhances binary classification by discovering latent architectural patterns within the "fake" class. TriDetect employs balanced cluster assignment via the Sinkhorn-Knopp algorithm and a cross-view consistency mechanism, encouraging the model to learn fundamental architectural distincts. We evaluate our approach on two standard benchmarks and three in-the-wild datasets against 13 baselines to demonstrate its generalization capability to unseen generators.

## Introduction

The rapid advancement of generative models (GMs), especially GANs (WhichFaceisReal 2019) and DMs (Huang et al. 2023), enables the creation of highly realistic synthetic images that are often indistinguishable from real photographs (Lu et al. 2023). While various detection methods have been proposed (Zhang, Karaman, and Chang 2019; Liu et al. 2021; Frank et al. 2020; Wang et al. 2023; Tan et al. 2025), their most critical limitation is the poor crossgenerator generalization (Deng et al. 2024; Shilin et al. 2025; Yan et al. 2025b; Chen et al. 2022). Cross-generator generalization, in this context, refers to the ability of a detector trained on one set of GMs to successfully identify images produced by models it has never encountered. This failure is particularly pronounced when crossing the boundaries of underlying architectural families, such as between

GANs and DMs. This generalization gap is a critical obstacle, as new generators constantly emerge in the real world (Nguyen-Le et al. 2025).

To address this generalization gap, the fundamental challenge lies in understanding why different architectural families produce systematically different patterns. Prior research has primarily explored that GANs and DMs leave surfacelevel artifacts in synthetic images, such as checkerboard patterns (Dzanic, Shah, and Witherden 2020; Zhang, Karaman, and Chang 2019; Frank et al. 2020; Wang et al. 2020a) and noise residuals (Wang et al. 2023; Ma et al. 2024). However, this approach faces an inherent limitation: these surfacelevel artifacts are vulnerable to simple post-processing operations, further limiting detection robustness. In contrast to prior work, we shift from analyzing surface-level artifacts to latent architectural patterns inherent to each generative architecture family. Specifically, we hypothesize that latent representations of synthetic images generated by GANs and DMs form significantly different submanifolds in feature space. This hypothesis stems from the fundamental observation that GANs and DMs have distinct optimization objectives, which fundamentally shape how these generative architecture families model data distribution: the Jensen-Shannon (JS) divergence is optimized by GANs, whereas the Kullback-Leibler (KL) divergence is minimized by DMs.

In this work, we demonstrate the existence of latent architectural patterns inherent to each generative architecture family (i.e., GANs and DMs) through a theoretical analysis of their optimization objectives. By utilizing the manifold hypothesis (Fefferman, Mitter, and Narayanan 2016; Loaiza-Ganem et al. 2024), we show that GANs and DMs interact with the data manifold differently: GANs permit partial manifold coverage, leading to boundary artifacts, while DMs enforce complete coverage, resulting in oversmoothing patterns. This theoretical disparity implies that GAN-generated and DM-generated images occupy distinct, separable submanifolds within a well-learned feature space (Fig. 2). This theoretical analysis directly guides our method design. Rather than attempting to detect specific generators or relying on surface-level patterns, we propose Triarchy **Detect**or (TriDetect), a novel semi-supervised method designed to recognize these fundamental architectural signatures. Specifically, TriDect simultaneously performs binary classification while discovering latent architectural pat-

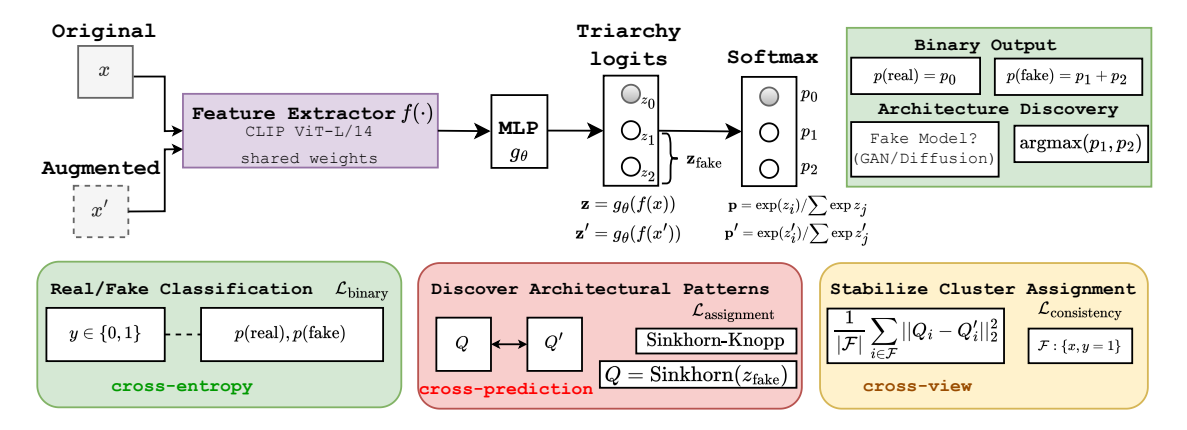


Figure 1: Overview of our proposed method, TriDetect.

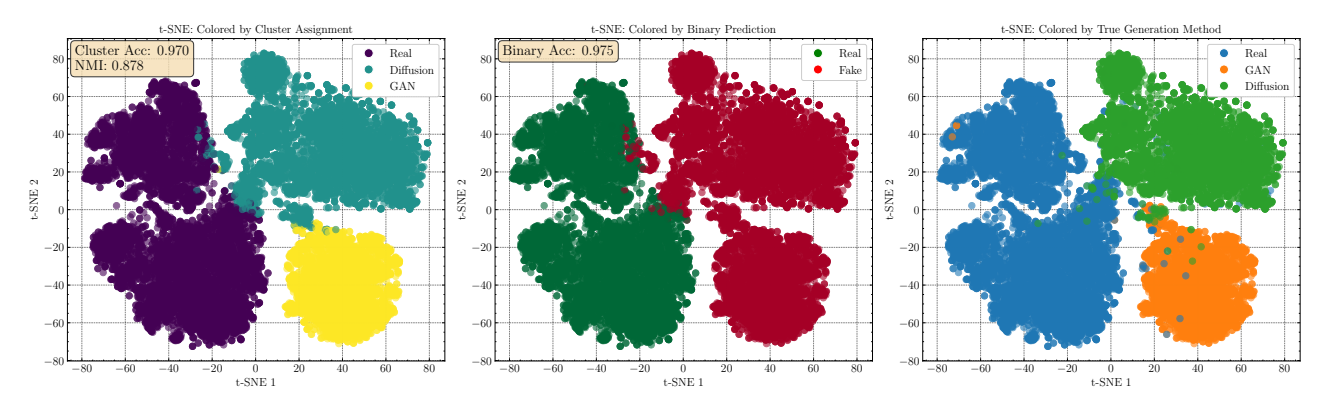


Figure 2: Visualization of learned representations demonstrating successful discovery of fake sub-types. The three t-SNE projections display feature embeddings colored by (left) the model's unsupervised cluster assignments, (middle) the model's binary real/fake predictions, and (right) the ground-truth generation methods. Results are performed on AIGCDetectBenchmark.

terns within the synthetic data (Fig. 1). To ensure robust learning, we employ the Sinkhorn-Knopp algorithm (Cuturi 2013) to enforce balanced cluster assignments, preventing cluster collapse. Furthermore, a cross-view consistency mechanism is designed to ensure the model learns fundamental architectural distinctions rather than image statistics. By discovering latent architectural patterns, our method can enhance the cross-generator generalization within the same architecture families.

## Main Contributions. Our contributions include:

- Theoretical Analysis: We provide the first theoretical explanation for why the GAN and DM architectures produce fundamentally different latent patterns, grounded in their optimization objectives and manifold coverage.
- Novel Semi-supervised Detection Method: We introduce TriDetect that combines binary classification with architecture-aware clustering to learn generalized architectural features.
- **Comprehensive Evaluation**: We evaluate on 5 datasets against 13 SoTA detectors, demonstrating superior crossgenerator and cross-dataset generalization.

## From Divergence to Detection: A Theoretical Analysis of Architectural Artifacts

In this section, we provide the theoretical analysis to demonstrate that latent representations of synthetic images generated by GANs and DMs form significantly different submanifolds in feature space. The t-SNE visualization in Figure 2 confirms this analysis. Specifically, our analysis reveals that these differences are fundamental consequences of their optimization targets. We begin by examining the optimization objectives of each architecture family, then demonstrate how these objectives lead to characteristic coverage patterns and to distinguishable artifacts.

#### The Fundamental Disparity in Optimization

We use  $p_{data}$ ,  $p_{GAN}$ , and  $p_{DM}$  to denote the data, GAN-generated, and DM-generated distributions, respectively.

**Lemma 1.** (DM Optimization Objective). Suppose that  $x_0 \sim p_{data}$ , DM minimizes an upper bound on the KL divergence between the data and model distributions:

 $D_{KL}(p_{data}||p_{DM}) \leq \mathbb{E}_{x_0 \sim p_{data}}[-ELBO(x_0)] - H(p_{data}),$  (1) where ELBO is the Evidence Lower Bound and  $H(p_{data})$  is the entropy of the data distribution.

Remark 1. (Equality Condition). The inequality in Lemma 1 becomes an equality when the variational posterior  $q(x_{1:T}|x_0)$  equals the true posterior  $p_{\rm DM}(x_{1:T}|x_0)$  under the model. In standard DMs, this condition can be achieved at the global optimum when the reverse process has sufficient capacity (Luo 2022), yielding:

$$D_{\mathrm{KL}}(p_{\mathrm{data}}||p_{\mathrm{DM}}) = \mathbb{E}_{x_0 \sim p_{\mathrm{data}}}[-\mathrm{ELBO}(x_0)] + H(p_{\mathrm{data}}) \quad (2)$$

Since  $H(p_{\rm data})$  is independent of model parameters, minimizing  $\mathbb{E}_{x_0 \sim p_{\rm data}}[-{\rm ELBO}(x_0)]$  is equivalent to minimizing  $D_{KL}(p_{\rm data}||p_{\rm DM})$ . Lemma 1 is supported by recent works on DMs (Luo 2022; Nichol and Dhariwal 2021), which indicates that DMs indirectly minimize the KL divergence by maximizing the ELBO. KL divergence is asymmetric and severely penalizes the model if  $p_{DM}=0$  where  $p_{data}>0$ .

**Lemma 2.** (GAN optimization problem) For a fixed generator  $\mathcal{G}$ , the value function  $V(\mathcal{D}, \mathcal{G})$  satisfies the inequality:

$$V(\mathcal{D}, \mathcal{G}) \le 2D_{JS}(p_{data} || p_{GAN}) - 2\log 2, \tag{3}$$

with equality if and only if the discriminator is optimal, given by  $\mathcal{D}^*(x) = p_{data}(x)/(p_{data}(x) + p_{GAN}(x))$ 

In contrast to DMs, GANs optimize the JS divergence through an adversarial game (Che et al. 2020; Goodfellow et al. 2020; Arjovsky, Chintala, and Bottou 2017). Unlike the KL divergence, the JS divergence is symmetric and remains bounded even when the generator completely ignores certain regions of the data space.

These lemmas lead to our first key theoretical result:

**Theorem 1.** (Fundamental Difference in Optimization Objectives) Using the notations of Lemmas 1 and 2, GANs and DMs solve various optimization problems:

- 1. GANs:  $\min_{\mathcal{G}} V(\mathcal{D}^*, \mathcal{G}) \equiv \min_{\mathcal{G}} D_{JS}(p_{data} || p_{GAN})$ , where  $\mathcal{D}^*$  is the optimal discriminator.
- 2. DMs:  $\min_{x \sim p_{data}} [-ELBO(x)] H(p_{data}) \equiv \min_{x \in D_{KL}} (p_{data} || p_{DM})$

Proof for Theorem 1 in Appendix. Theorem 1 indicates the fundamental difference between the optimization objectives of GANs and DMs.

## From Divergence to Distribution Support and Artifacts

The choice of divergence profoundly impacts the learned distributions and the nature of artifacts inherent to the generation process.

**Theorem 2.** (Disparity of Learned Distribution Support) Let  $p_{data}$  be the true data distribution with support  $S_{data} = \{x : p_{data}(x) > 0\}$ . Assume that the generator and score-matching networks have sufficient capacity:

1. **GANs**: A globally optimal solution for the GAN generator, which minimizes the JS divergence  $D_{JS}(p_{data}||p_{GAN})$ , can exist even if the support of the learned distribution,  $S_{GAN}$ , is a strict subset of the data support ( $S_{GAN} \subset S_{data}$ , partial coverage).

2. **DMs**: A globally optimal solution for the DM, which minimizes the upper bound on the KL divergence  $D_{KL}(p_{data}||p_{DM})$ , requires the support of the learned distribution,  $S_{DM}$ , to cover the support of the data distribution ( $S_{data} \subseteq S_{DM}$ , complete coverage).

Proof in Appendix. Theorem 2 reveals why GANs and DMs exhibit fundamentally different coverage behaviors. For DMs, to achieve an optimal solution, the support of its learned distribution must cover the support of the real data distribution ( $S_{\text{data}} \subseteq S_{\text{DM}}$ ). This is because the KL divergence  $D_{KL}(p_{data}||p_{DM})$  becomes infinite whenever  $p_{DM} = 0$ for any x where  $p_{\rm data}>0$ . As a result, DMs must spread their capacity across the entire data manifold, resulting in diffusion blur, over-smoothing in low-density regions. Furthermore, the iterative denoising process of DMs relies on score matching. Imperfections in this estimation accumulate during the reverse diffusion steps, combined with the smoothing enforced by the KL objective, will leave unique, structured noise residuals that serve as a distinct architectural artifact (Wang et al. 2023; Ma et al. 2024). In contrast, due to JS divergence optimization, GANs can achieve optimality while ignoring low-probability regions of  $p_{\text{data}}$ . This leads to sharp samples but incomplete coverage where GANs concentrate their capacity on high-density modes, producing sharp samples but missing rare patterns. The boundary artifacts manifest as abrupt transitions at the edges of learned support, creating detectable discontinuities. These discontinuities manifest in the image space as characteristic boundary artifacts, such as structural inconsistencies or unnatural texture transitions (Zhang, Karaman, and Chang 2019).

## Methodology

This section presents a semi-supervised **Tri**rchy **Detector** (TriDetect) that simultaneously performs binary classification and discovers latent structures within synthetic images. From our theoretical analysis, by learning to recognize distinct architectural patterns that persist across specific generators within each family (i.e., GANs vs. DMs), it is possible to achieve cross-generator generalization capability.

## **Problem Formulation and Objectives**

Given a dataset  $\mathcal{D}=\{(x_i,y_i)\}_{i=1}^N$  where  $x_i\in\mathbb{R}^{H\times W\times 3}$  represents an image and  $y_i\in\{0,1\}$  denotes its binary label (0:real, 1:fake), we compute logits  $z_i=g_{\theta}(f(x_i))\in\mathbb{R}^3$  using a fine-tuned vision encoder f and classifier  $g_{\theta}$ , where we have 3 output dimensions (one real class and two fake clusters). We formulate a joint optimization problem with two objectives: (i) distinguish real from synthetic images, and (ii) automatically discover latent clusters within synthetic samples that correspond to different generative architectures. The architecture produces three-way logits that align with the theoretical distinction between GAN and DM architectures established in our analysis.

#### **Balanced Clustering via Optimal Transport**

A critical challenge in unsupervised deep clustering is the tendency toward trivial solutions where all samples collapse into a single cluster (Zhou et al. 2024). This problem is particularly serious in our setting, where we seek to discover subtle architectural patterns within synthetic images generated by different generators. To address this, we formulate cluster assignment as an optimal transport problem that enforces balanced distribution across clusters.

For a batch B of synthetic samples with logits  $Z_{\text{fake}} \in \mathbb{R}^{B \times K}$  where K=2 is the number of fake clusters, we seek an assignment matrix  $Q \in \mathbb{R}^{B \times K}$  that maximizes the similarity between samples and clusters while maintaining balanced assignments:

$$\max_{Q \in \mathcal{O}} \operatorname{Tr}(Q^T Z_{\text{fake}}) + \epsilon H(Q), \tag{4}$$

where  $H(Q) = -\sum_{ij} Q_{ij} \log Q_{ij}$  is the entropy function,  $\epsilon$  controls assignment smoothness, and Q is the transportation polytope (Asano, Rupprecht, and Vedaldi 2019):

$$Q = \left\{ Q \in \mathbb{R}_+^{B \times K} \mid Q \mathbf{1}_K = \mathbf{1}_B, \ Q^T \mathbf{1}_B = \frac{B}{K} \mathbf{1}_K \right\}$$
 (5)

These constraints ensure that each sample is fully assigned across clusters (rows sum to 1) and each cluster receives exactly B/K samples (columns sum to B/K), preventing collapse.

Sinkhorn-Knopp Algorithm for Online Clustering. We utilize the Sinkhorn-Knopp algorithm (Cuturi 2013) to solve the optimal transport problem. Starting from the initialization  $Q^{(0)} = \exp(Z_{\text{fake}}/\epsilon)$ , for  $t=1,\ldots,T$  iterations, we perform:

$$Q^{(t)} = \mathcal{R}(Q^{(t-1)}); \quad Q^{(t)} = \mathcal{C}(Q^{(t)}),$$
 (6)

where  $\mathcal{R}(Q)_{ij} = \frac{Q_{ij}}{\sum_k Q_{ik}}$  normalizes rows and  $\mathcal{C}(Q)_{ij} = \frac{K \cdot Q_{ij}}{\sum_k Q_{kj}}$  normalizes columns with appropriate scaling to maintain the balance constraints. Note that Eq. 6 is operated on mini-batches rather than the entire dataset, enabling online learning that scales to arbitrarily large datasets.

### **Cross-view Consistency for Generalized Learning**

To learn discriminative and generalized clusters that capture architectural patterns rather than image statistics, we propose a cross-view consistency mechanism that encourages consistent predictions and clustering stability. This mechanism contains the *swapped prediction strategy* and *consistency regularization*.

Swapped Prediction for Cluster Learning. Let (x,x') denote different views, generated by random transformations on each image, with corresponding logits (z,z'). For fake samples, we extract the fake cluster logits  $z_{\rm fake}$  and  $z'_{\rm fake}$ . Inspired by the work (Caron et al. 2020), the core idea here is to use the cluster assignment from one view to supervise the prediction from the other view. Specifically, after computing balanced assignments using the Sinkhorn-Knopp algorithm  $Q={\rm Sinkhorn}(z_{\rm fake})$  and  $Q'={\rm Sinkhorn}(z'_{\rm fake})$  for fake samples in each view, the assignment loss is computed as follows:

$$\mathcal{L}_{\text{assignment}} = -\frac{1}{2|\mathcal{F}|} \sum_{i \in \mathcal{F}} \left( \sum_{k=1}^{K} Q'_{ik} \log p_{ik} + \sum_{k=1}^{K} Q_{ik} \log p'_{ik} \right), \quad (7)$$

## Algorithm 1: TriDetect Training Algorithm

**Require:** Dataset  $\mathcal{D} = \{(x_i, y_i)\}_{i=1}^N$ , feature encoder f, classifier  $g_\theta$ , learning rate  $\eta$ , hyperparameters  $\beta, \omega_1, \omega_2, K = 2$  (fake clusters)

```
Ensure: Trained encoder f and classifier g_{\theta}
  1: Initialize classifier parameters \theta
  2: for t = 1 to T epochs do
                 for each batch \mathcal{B} \subset \mathcal{D} do
                          \mathcal{B}' \leftarrow \operatorname{Augment}(\mathcal{B}) \qquad \triangleright \operatorname{Create} \text{ augmented views } \\ Z, Z' \leftarrow g_{\theta}(f(\mathcal{B})), g_{\theta}(f(\mathcal{B}')) \qquad \triangleright \operatorname{Compute} \text{ triarchy}
  4:
  5:
         logits
                          6:
  7:
          fake logits
  8:
                           Q_{\text{fake}}, Q'_{\text{fake}} \leftarrow \text{Sinkhorn}(Z_{\text{fake}}), \text{Sinkhorn}(Z'_{\text{fake}})
          Balanced assignment
                           Compute \mathcal{L}_{binary} (Eq.10), \mathcal{L}_{assignment} (Eq.7), \mathcal{L}_{consistency}
          (Eq.8)
                           \begin{split} & \mathcal{L}_{\text{cluster}} \leftarrow \omega_1 \mathcal{L}_{\text{assignment}} + \omega_2 \mathcal{L}_{\text{consistency}} \\ & \mathcal{L}_{\text{total}} \leftarrow \beta \mathcal{L}_{\text{binary}} + (1-\beta) \mathcal{L}_{\text{cluster}} \\ & \theta \leftarrow \theta - \eta \nabla_{\theta} \mathcal{L}_{\text{total}} \quad \quad \triangleright \text{Update parameters} \end{split} 
10:
11:
12:
                   end for
13:
14: end for
15: return f, g_{\theta}
```

where  $\mathcal{F}$  denotes the set of fake samples in the batch and  $p_{ik} = \frac{\exp(z_{ik}/\tau)}{\sum_{j} \exp(z_{ij}/\tau)}$  with temperature  $\tau$ .

Consistency Regularization for Stable Assignments. The consistency regularization ensures that the Sinkhorn-Knopp assignments themselves remain stable across views, preventing oscillation during training and encouraging convergence to meaningful clusters. Particularly, this additional regularization directly constrains the similarity of assignments themselves:

$$\mathcal{L}_{\text{consistency}} = \frac{1}{|\mathcal{F}|} \sum_{i \in \mathcal{F}} ||Q_i - Q_i'||_2^2$$
 (8)

### **Loss Function**

The overall loss function for training TriDetect contains the binary classification loss and the clustering loss:

$$\mathcal{L}_{\text{total}} = \beta \mathcal{L}_{\text{binary}} + (1 - \beta) \mathcal{L}_{\text{cluster}}, \tag{9}$$

where  $\mathcal{L}_{\text{cluster}} = \omega_1 \mathcal{L}_{\text{assignment}} + \omega_2 \mathcal{L}_{\text{consistency}}$ .  $\beta$  denotes the hyperparameter that balances the importance of the binary and clustering losses while  $\omega_1$  and  $\omega_2$  represent assignment and consistency weights.  $\mathcal{L}_{\text{binary}}$  is the cross-entropy loss, computed as:

$$\mathcal{L}_{\text{binary}} = -\frac{1}{N} \sum_{i=1}^{N} [y_i \log p(\text{fake})_i + (1 - y_i) \log p(\text{real})_i],$$
(10)

where  $p_i = \operatorname{softmax}(z_i) \in \mathbb{R}^3$ , with  $p(\operatorname{real})_i = p_{i,0}$  and  $p(\operatorname{fake})_i = p_{i,1} + p_{i,2}$ . We provide the training pseudocode in Alg. 1 and the Sinkhorn-Knopp algorithm in Appendix.

Table 1: Comparison on the GenImage (Zhu et al. 2023) Dataset in terms of AUC Performance. The best result and the second-best result are marked in **bold** and underline, respectively.

Method	BigGAN	SD v1.4	ADM	GLIDE	MidJourney	VQDM	Wukong	Avg
CNNSpot	1.0000	0.9999	0.8139	0.9591	0.7969	0.8028	0.9988	0.9102
FreDect	1.0000	0.9970	0.7485	0.7713	0.7458	0.8086	0.9894	0.8658
Fusing	0.9999	0.9999	0.7261	0.5664	0.6671	0.7586	0.9988	0.8167
LGrad	0.6530	0.5623	0.5237	0.6103	0.5411	0.5244	0.6043	0.5742
LNP	0.9812	0.9809	0.6090	0.6089	0.6596	0.6825	0.9689	0.7844
CORE	1.0000	0.9998	0.8198	0.9950	0.8011	0.8192	0.9971	0.9189
SPSL	0.9998	0.9970	0.5946	0.8283	0.7545	0.7742	0.9918	0.8486
UIA-ViT	1.0000	0.9993	0.7314	0.9519	0.8024	0.7950	0.9946	0.8964
DIRE	0.9996	0.9997	0.8257	0.9843	0.8298	0.8303	0.9965	0.9237
UnivFD	0.9988	0.9955	0.9265	0.9920	0.9262	0.9859	0.9678	0.9704
AIDE	0.9998	0.9900	0.7736	0.9299	0.8680	0.8739	0.9710	0.9152
NPR	0.9999	0.9979	0.9385	0.9956	0.9430	0.9553	0.9861	0.9695
Effort	1.0000	1.0000	0.9052	0.9893	0.9795	0.9969	0.9998	0.9815
TriDetect	1.0000	1.0000	0.9609	0.9993	0.9581	0.9992	0.9999	0.9882

Table 2: Comparison on the AIGCDetectBenchmark (Zhong et al. 2023) Dataset in terms of AUC Performance. The best result and the second-best result are marked in **bold** and underline, respectively.

Method	SeeGAN	$s_{\theta'}e_{\mathcal{C}_{A,V}}$	Spiecarz	A POGAN	Gaucs.	Starce AV	Big CAN	МОР	Nakong	Chide	Ags	Mood	MidJourney	80 V.4	s <sub>14</sub> q <sub>8</sub>	DALLEZ	₹.
CNNSpot	0.3491	0.5298	0.4787	0.5039	0.4260	0.5538	0.3811	0.8138	0.9988	0.9591	0.8252	0.8028	0.7969	0.9999	0.9995	0.9748	0.7121
FreDect	0.3956	0.6697	0.6815	0.7172	0.5877	0.7211	0.8346	0.7485	0.9894	0.7713	0.8743	0.8086	0.7458	0.9970	0.9956	0.8224	0.7725
Fusing	0.4071	0.5180	0.5274	0.4797	0.4815	0.5072	0.3888	0.7261	0.9988	0.9429	0.7468	0.7586	0.6673	0.9999	0.9998	0.9448	0.6934
LGrad	0.4833	0.4783	0.4181	0.4993	0.4508	0.4925	0.4972	0.5317	0.6009	0.6758	0.4593	0.5100	0.5320	0.5639	0.5617	0.6041	0.5224
LNP	0.3984	0.5118	0.4842	0.4993	0.4884	0.4283	0.4246	0.6089	0.9689	0.8474	0.7127	0.6823	0.6596	0.9809	0.9800	0.8382	0.6571
CORE	0.6153	0.6115	0.5762	0.5617	0.5310	0.9731	0.5574	0.8198	0.9971	0.9950	0.7561	0.8193	0.8011	0.9998	0.9997	0.9498	0.7852
SPSL	0.5817	0.5384	0.5305	0.5252	0.5209	0.5228	0.6458	0.5946	0.9918	0.8283	0.8257	0.7742	0.7545	0.9971	0.9953	0.8301	0.7161
UIA-ViT	0.5291	0.7081	0.7545	0.5109	0.4934	0.5252	0.6471	0.7314	0.9946	0.9519	0.9358	0.7950	0.8024	0.9993	0.9988	0.8187	0.7623
DIRE	0.6335	0.5967	0.6117	0.7896	0.4016	0.9935	0.5755	0.8257	0.9965	0.9843	0.8928	0.8303	0.8298	0.9997	0.9995	0.9627	0.8077
UnivFD	0.9664	0.7297	0.7304	0.9407	0.9828	0.9185	0.9712	0.9265	0.9678	0.9920	0.9610	0.9859	0.9262	0.9955	0.9953	0.9627	0.9345
AIDE	0.6142	0.7377	0.7249	0.7979	0.8443	0.7025	0.8084	0.7736	0.9710	0.9299	0.9309	0.8739	0.8680	0.9900	0.9900	0.8859	0.8402
NPR	0.9288	0.8851	0.9403	0.9653	0.5391	0.9998	0.7939	0.9385	0.9861	0.9956	0.9728	0.9553	0.9430	0.9979	0.9967	0.9935	0.9270
Effort	0.9894	0.9431	0.8961	0.9973	0.9997	0.9923	0.9991	0.9052	0.9998	0.9893	0.9980	0.9969	0.9795	1.0000	1.0000	0.9666	0.9783
TriDetect	1.0000	0.9419	0.9422	0.9995	0.9978	1.0000	0.9992	0.9609	0.9999	0.9993	0.9948	0.9992	0.9581	1.0000	1.0000	0.9971	0.9869

## **Experiments**

#### **Experimental Setup**

**Baselines.** We compare our method against 13 competitive detectors, including CNNSpot (Wang et al. 2020b), LNP (Liu et al. 2022), FreDect (Frank et al. 2020), CORE (Ni et al. 2022), SPSL (Liu et al. 2021), UIA-ViT (Zhuang et al. 2022), Fusing (Ju et al. 2022), LGrad (Tan et al. 2023), DIRE (Wang et al. 2023), UnivFD (Ojha, Li, and Lee 2023), AIDE (Shilin et al. 2025), NPR (Tan et al. 2025), and Effort (Yan et al. 2025b).

**Datasets.** We evaluate our method on 2 standard benchmarks (GenImage (Zhu et al. 2023), AIGCDetectBenchmark (Zhong et al. 2023)) and 3 in-the-wild datasets (Wild-Fake (Hong et al. 2025), Chameleon (Shilin et al. 2025), DF40 (Yan et al. 2024)). In our experiments, we follow the training protocol introduced by (Shilin et al. 2025) by utilizing BigGAN and SDv1.4 subsets of GenImage.

**Metrics.** In this work, we report results across 4 commonly used metrics: accuracy (ACC), area under the ROC curve (AUC), equal error rate (EER), and average precision (AP). We primarily report AUC and ACC in the main paper; other metric results are provided in Appendix.

**Implementation Details.** We use CLIP ViT-L/14 (Radford et al. 2021) vision encoder f, which is fine-tuned with Low-Rank Adaptation (LoRA) (Hu et al. 2022). For baseline implementation, we use two benchmarks, DeepfakeBench (Yan et al. 2023) and AIGCDetectBenchmark (Zhong et al. 2023). Detailed experimental procedures, hyperparameters, and configurations are provided in Appendix.

#### **Experimental Results**

**Standard Benchmarks.** On GenImage, Table 1 shows that TriDetect achieves the highest average AUC of 0.9882, outperforming SoTA methods, including AIDE (0.9152), NPR (0.9695), and Effort (0.9815). The results on AIGCDe-

Table 3: Comparison on the WildFake (Hong et al. 2025) Dataset in terms of ACC Performance. The best result and the second-best result are marked in **bold** and underline, respectively.

Method	DALL-E	DDIM	DDPM	VQDM	BigGAN	StarGAN	StyleGAN	DF-GAN	GALIP	GigaGAN	Avg
CNNSpot	0.5961	0.2929	0.2811	0.2882	0.8456	0.3350	0.3453	0.3418	0.3325	0.3409	0.3999
FreDect	0.4078	0.2817	0.2952	0.4643	0.8415	0.3689	0.3365	0.4415	0.3478	0.8148	0.4600
Fusing	0.4706	0.2376	0.2427	0.3305	0.9361	0.3425	0.3361	0.3518	0.3587	0.3446	0.3951
LGrad	0.6044	0.5794	0.5473	0.5656	0.6126	0.5517	0.5129	0.5732	0.4796	0.5758	0.5602
LNP	0.5105	0.2681	0.2715	0.3580	0.7179	0.3741	0.3696	0.3697	0.3649	0.3708	0.3975
CORE	0.3829	0.2552	0.2762	0.3668	0.7115	0.3359	0.3353	0.3974	0.3365	0.3400	0.3738
SPSL	0.5614	0.2282	0.2535	0.3082	0.8692	0.3324	0.3395	0.3618	0.3338	0.3334	0.3921
UIA-ViT	0.5718	0.2699	0.2636	0.3475	0.7542	0.3402	0.3635	0.3806	0.3430	0.3592	0.3993
DIRE	0.5725	0.3222	0.3130	0.4370	0.6130	0.3885	0.3465	0.3941	0.3724	0.3755	0.4135
UnivFD	0.5492	0.8244	0.7536	0.7974	0.7962	0.6213	0.5734	0.9141	0.8572	0.7690	0.7456
AIDE	0.5806	0.3562	0.3405	0.4757	0.7420	0.3948	0.4331	0.6638	0.4215	0.3647	0.4773
NPR	0.5122	0.6892	0.5305	0.7313	0.7102	0.5510	0.3583	0.7753	0.5221	0.6876	0.6068
Effort	0.6741	0.6436	0.4800	0.8467	0.8992	0.7971	0.6027	0.9767	0.8127	0.7891	0.7522
TriDetect	0.6021	0.7359	0.7207	0.9301	0.8042	0.9998	0.6300	0.9825	0.9017	0.9468	0.8254

Table 4: Comparison on the DF40 (Yan et al. 2024) Dataset in terms of ACC Performance. The best result and the second-best result are marked in **bold** and underline, respectively.

Method	CollabDiff	MidJourney	DeepFaceLab	StarGAN	StarGAN2	StyleCLIP	WhichisReal	Avg
CNNSpot	0.5635	0.5376	0.3808	0.4851	0.5040	0.3041	0.5012	0.4681
FreDect	0.8720	0.4614	0.3322	0.4982	0.5158	0.4103	0.5327	0.5175
Fusing	0.6150	0.5296	0.4830	0.4554	0.4942	0.2908	0.4978	0.4808
LGrad	0.5045	0.5019	0.5374	0.5088	0.4670	0.6124	0.5107	0.5204
LNP	0.5120	0.4997	0.3808	0.4962	0.5108	0.3428	0.5292	0.4674
CORE	0.5025	0.5328	0.5708	0.5000	0.5000	0.2612	0.4998	0.4810
SPSL	0.5140	0.5280	0.3337	0.4955	0.4992	0.2884	0.4988	0.4511
UIA-ViT	0.5380	0.4374	0.3609	0.5033	0.5008	0.3930	0.4698	0.4576
DIRE	0.5070	0.5424	0.3275	0.5000	0.5000	0.2652	0.4658	0.4440
UnivFD	0.5955	0.7304	0.5369	0.6361	0.5516	0.8353	0.6727	0.6512
NPR	0.4995	0.8711	0.3228	0.4970	0.5000	0.2610	0.6442	0.5136
AIDE	0.5525	0.7038	0.4039	0.6331	0.5055	0.4066	0.5197	0.5322
Effort	0.9735	0.8370	0.4500	0.9287	0.7345	0.9710	0.8291	0.8177
TriDetect	0.9690	0.8629	0.6402	0.8005	0.8208	0.9825	0.8241	0.8429

tectBenchmark (Table 2) also demonstrate the generalization capability of TriDetect to 16 unseen generators, yielding an improvement over DIRE (22.18%), AIDE (17.4%), UnivFD (5.6%), NPR (6.5%), and Effort (0.9%).

**In-the-wild Datasets.** Tables 3-5 show that our method outperforms existing detectors across all evaluation metrics on in-the-wild datasets:

- Robust to degradation techniques: TriDetect exhibits consistent performance when evaluated on WildFake in which degradation techniques (e.g., downsampling, cropping) are applied on testing sets. Particularly, TriDetect achieves an average ACC of 0.8254, a 8.86% improvement compared to Effort. Results demonstrate the better robustness of TriDetect than other methods.
- **Generalize to facial editing methods:** On DF40 dataset, TriDetect achieves an average ACC of 0.8429, an improvement of 3.08% and 29.43% compared to Effort and UnivFD, respectively.

• Achieve lowest EER: On the challenging Chameleon dataset (Table 5), which is designed to deceive both humans and AI models, TriDetect attains the lowest EER of 0.1843, a 31.74% reduction compared to Effort. This demonstrates that our approach can achieve a superior balance between false positive and false negative rates.

## **Ablation Study**

#### **Module Ablation of Components in TriDetect**

Table 6 provides evidence for the contribution of each loss component in our TriDetect. With  $\mathcal{L}_{assignment}$  and  $\mathcal{L}_{consistency}$ , TriDetect can yield a substantial improvement in AUC to 0.8935 and ACC to 0.6258. These results highlight the significant contribution of the clustering loss to TriDetect's performance.

Table 5: Comparison on the Chameleon (Shilin et al. 2025) Dataset in terms of AUC, ACC, EER, and AP Performance. The best result and the second-best result are marked in **bold** and underline, respectively.

Method	AUC	ACC	EER	AP
CNNSpot	0.6331	0.5838	0.4062	0.5800
FreDect	0.7545	0.6304	0.3143	0.6864
Fusing	0.6020	0.5745	0.4138	0.5350
LGrad	0.5342	0.5155	0.4809	0.4735
LNP	0.5798	0.5790	0.4420	0.5039
CORE	0.5264	0.5700	0.4772	0.4556
SPSL	0.6135	0.5748	0.4147	0.5335
UIA-ViT	0.7042	0.5987	0.3538	0.6115
DIRE	0.5488	0.5768	0.4565	0.4909
UnivFD	0.8030	0.6598	0.2670	0.7506
AIDE	0.7970	0.6256	0.2747	0.7345
NPR	0.5865	0.5805	0.4381	0.4943
Effort	0.8371	0.6459	0.2428	0.7692
TriDetect	0.8935	0.6788	0.1843	0.8742

Table 6: Ablation study on the binary classification loss ( $\mathcal{L}_{\text{binary}}$ ), assignment loss ( $\mathcal{L}_{\text{assignment}}$ ), and consistency loss ( $\mathcal{L}_{\text{consistency}}$ ). Results are performed on Chameleon dataset.

$\mathcal{L}_{ ext{binary}}$	$\mathcal{L}_{assignment}$	$\mathcal{L}_{ ext{consistency}}$	AUC	ACC	EER	AP
<b>√</b>			0.8033	0.6335	0.2713	0.7503
$\checkmark$	✓		0.8560	0.5817	0.2195	0.8394
$\checkmark$	✓	✓	0.8935	0.6258	0.1843	0.8742

## **Different Values of** $\beta$

The ablation study on  $\beta$  (Table 7) reveals a crucial insight: the optimal balance between binary classification and clustering objectives occurs at  $\beta=0.7$ , where the model achieves peak performance across all metrics.

#### **Analysis on Learned Embedding Spaces**

Figure 2 provides visual evidence that TriDetect successfully discovers meaningful latent structure within synthetic images. The alignment between unsupervised discovery (left figure) and ground truth (right figure) validates our theoretical analysis that different generative architectures leave distinguishable artifacts in feature space. The middle figure further confirms that this clustering capability enhances rather than compromises binary detection performance.

We also provide other ablation studies in Appendix, including comparison with attribution baselines and ablation study on different numbers of fake clusters. Results show that TriDetect outperforms the selected attribution baselines, and K=2 is the optimal number of fake clusters.

## **Related Work**

### **Generalized AI-generated Image Detection**

AI-generated images exhibit artifacts throughout the entire scene. The detection landscape encompasses three primary approaches: data augmentations for improved generalization

Table 7: Ablation studies on  $\beta$  value in our method. Results are performed on Chameleon dataset.

$\beta$ value	AUC	ACC	EER	AP
$\beta = 0.3$	0.8423	0.6069	0.2348	0.8147
$\beta = 0.5$	0.8451	0.5994	0.2338	0.8058
$\beta = 0.7$	0.8935	0.6258	0.1843	0.8742
$\beta = 0.9$	0.8774	0.6043	0.2033	0.8713

(Wang et al. 2020b), artifact analysis techniques identifying generation-specific patterns such as GAN checkerboard artifacts (Zhang, Karaman, and Chang 2019; Tan et al. 2025) and diffusion reconstruction errors (Luo et al. 2024; Wang et al. 2023), and vision-language models leveraging CLIP representations to capture subtle synthetic patterns (Ojha, Li, and Lee 2023; Yan et al. 2025a,b). Recent advances include the exploitation of upsampling traces common to both GANs and DMs (Tan et al. 2025), while adaptation strategies employ meta-learning (Chen et al. 2022), and incremental learning (Pan et al. 2023) to address evolving generators.

Compared to these works, we provide the first theoretical explanation for distinct artifacts left by GANs and DMs. These theoretical results motivate us to design TriDetect that simultaneously performs binary detection and discovers architectural patterns without explicit supervision.

### **Deep Clustering**

Deep clustering has evolved from multi-stage pipelines separating representation learning and clustering (Tao, Takagi, and Nakata 2021; Zhang et al. 2021; Peng et al. 2016) to end-to-end approaches jointly optimizing both objectives (Ji et al. 2021; Shen et al. 2021; Caron et al. 2020; Qian 2023). Notable advances include utilizing the Sinkhorn-Knopp algorithm for optimal cluster assignment through prototype matching (Caron et al. 2020) and designing hardness-aware objectives for training stability (Qian 2023).

While our method also employs Sinkhorn-Knopp, we uniquely combine it with semi-supervised learning to leverage real image supervision while discovering architectural patterns in synthetic images. We also propose a consistency regularization loss to ensure stable cluster assignment.

#### Conclusion

This work provides the first theoretical analysis to demonstrate that latent representations of synthetic images generated by GANs and DMs form significantly different submanifolds in feature space. This analysis motivates TriDetect, a semi-supervised detection method that enhances binary classification with architecture-aware clustering. Through discovering latent architectural patterns without explicit labels, TriDetect can learn more generalized representations that help to improve the generalization capabilities across unseen generators within the same architecture families. This work establishes a new paradigm for AI-generated image detection, shifting from pattern recognition to architectural understanding, providing a foundation for addressing future generators.

## Acknowledgments

This work was funded by Taighde Éireann – Research Ireland through the Research Ireland Centre for Research Training in Machine Learning (18/CRT/6183).

#### References

- Arjovsky, M.; Chintala, S.; and Bottou, L. 2017. Wasserstein generative adversarial networks. In *International conference on machine learning*, 214–223. PMLR.
- Asano, Y. M.; Rupprecht, C.; and Vedaldi, A. 2019. Self-labelling via simultaneous clustering and representation learning. *arXiv preprint arXiv:1911.05371*.
- Brock, A.; Donahue, J.; and Simonyan, K. 2018. Large scale GAN training for high fidelity natural image synthesis. *arXiv preprint arXiv:1809.11096*.
- Caron, M.; Misra, I.; Mairal, J.; Goyal, P.; Bojanowski, P.; and Joulin, A. 2020. Unsupervised learning of visual features by contrasting cluster assignments. *Advances in neural information processing systems*, 33: 9912–9924.
- Che, T.; Zhang, R.; Sohl-Dickstein, J.; Larochelle, H.; Paull, L.; Cao, Y.; and Bengio, Y. 2020. Your GAN is secretly an energy-based model and you should use discriminator driven latent sampling. *Advances in Neural Information Processing Systems*, 33: 12275–12287.
- Chen, L.; Zhang, Y.; Song, Y.; Wang, J.; and Liu, L. 2022. Ost: Improving generalization of deepfake detection via one-shot test-time training. *Advances in Neural Information Processing Systems*, 35: 24597–24610.
- Choi, Y.; Choi, M.; Kim, M.; Ha, J.-W.; Kim, S.; and Choo, J. 2018. Stargan: Unified generative adversarial networks for multi-domain image-to-image translation. In *Proceedings of the IEEE conference on computer vision and pattern recognition*, 8789–8797.
- Choi, Y.; Uh, Y.; Yoo, J.; and Ha, J.-W. 2020. Stargan v2: Diverse image synthesis for multiple domains. In *Proceedings of the IEEE/CVF conference on computer vision and pattern recognition*, 8188–8197.
- Cover, T. M. 1999. *Elements of information theory*. John Wiley & Sons.
- Cuturi, M. 2013. Sinkhorn distances: Lightspeed computation of optimal transport. *Advances in neural information processing systems*, 26.
- DeepFaceLab. -. DeepFaceLab. [Accessed 31-07-2025].
- Deng, J.; Guo, J.; Xue, N.; and Zafeiriou, S. 2019. Arcface: Additive angular margin loss for deep face recognition. In *Proceedings of the IEEE/CVF conference on computer vision and pattern recognition*, 4690–4699.
- Deng, J.; Lin, C.; Zhao, Z.; Liu, S.; Peng, Z.; Wang, Q.; and Shen, C. 2024. A survey of defenses against ai-generated visual media: Detection, disruption, and authentication. *ACM Computing Surveys*.
- Dhariwal, P.; and Nichol, A. 2021. Diffusion models beat gans on image synthesis. *Advances in neural information processing systems*, 34: 8780–8794.

- Dzanic, T.; Shah, K.; and Witherden, F. 2020. Fourier spectrum discrepancies in deep network generated images. *Advances in neural information processing systems*, 33: 3022–3032.
- Fefferman, C.; Mitter, S.; and Narayanan, H. 2016. Testing the manifold hypothesis. *Journal of the American Mathematical Society*, 29(4): 983–1049.
- Frank, J.; Eisenhofer, T.; Schönherr, L.; Fischer, A.; Kolossa, D.; and Holz, T. 2020. Leveraging frequency analysis for deep fake image recognition. In *International conference on machine learning*, 3247–3258. PMLR.
- Goodfellow, I.; Pouget-Abadie, J.; Mirza, M.; Xu, B.; Warde-Farley, D.; Ozair, S.; Courville, A.; and Bengio, Y. 2020. Generative adversarial networks. *Communications of the ACM*, 63(11): 139–144.
- Gu, S.; Chen, D.; Bao, J.; Wen, F.; Zhang, B.; Chen, D.; Yuan, L.; and Guo, B. 2022. Vector quantized diffusion model for text-to-image synthesis. In *Proceedings of the IEEE/CVF conference on computer vision and pattern recognition*, 10696–10706.
- Hong, Y.; Feng, J.; Chen, H.; Lan, J.; Zhu, H.; Wang, W.; and Zhang, J. 2025. Wildfake: A large-scale and hierarchical dataset for ai-generated images detection. In *Proceedings of the AAAI Conference on Artificial Intelligence*, volume 39, 3500–3508.
- Hu, E. J.; Wallis, P.; Allen-Zhu, Z.; Li, Y.; Wang, S.; Wang, L.; Chen, W.; et al. 2022. LoRA: Low-Rank Adaptation of Large Language Models. In *International Conference on Learning Representations*.
- Huang, Z.; Chan, K. C.; Jiang, Y.; and Liu, Z. 2023. Collaborative diffusion for multi-modal face generation and editing. In *Proceedings of the IEEE/CVF conference on computer vision and pattern recognition*, 6080–6090.
- Ji, Q.; Sun, Y.; Hu, Y.; and Yin, B. 2021. Variational deep embedding clustering by augmented mutual information maximization. In 2020 25th International Conference on Pattern Recognition (ICPR), 2196–2202. IEEE.
- Ju, Y.; Jia, S.; Ke, L.; Xue, H.; Nagano, K.; and Lyu, S. 2022. Fusing global and local features for generalized aisynthesized image detection. In 2022 IEEE International Conference on Image Processing (ICIP), 3465–3469. IEEE.
- Kang, M.; Zhu, J.-Y.; Zhang, R.; Park, J.; Shechtman, E.; Paris, S.; and Park, T. 2023. Scaling up gans for text-to-image synthesis. In *Proceedings of the IEEE/CVF conference on computer vision and pattern recognition*, 10124–10134.
- Karras, T.; Aila, T.; Laine, S.; and Lehtinen, J. 2017. Progressive growing of gans for improved quality, stability, and variation. *arXiv preprint arXiv:1710.10196*.
- Karras, T.; Laine, S.; and Aila, T. 2019. A style-based generator architecture for generative adversarial networks. In *Proceedings of the IEEE/CVF conference on computer vision and pattern recognition*, 4401–4410.
- Karras, T.; Laine, S.; Aittala, M.; Hellsten, J.; Lehtinen, J.; and Aila, T. 2020. Analyzing and improving the image quality of stylegan. In *Proceedings of the IEEE/CVF conference on computer vision and pattern recognition*, 8110–8119.

- Liu, B.; Yang, F.; Bi, X.; Xiao, B.; Li, W.; and Gao, X. 2022. Detecting generated images by real images. In *European Conference on Computer Vision*, 95–110. Springer.
- Liu, H.; Li, X.; Zhou, W.; Chen, Y.; He, Y.; Xue, H.; Zhang, W.; and Yu, N. 2021. Spatial-phase shallow learning: rethinking face forgery detection in frequency domain. In *Proceedings of the IEEE/CVF conference on computer vision and pattern recognition*, 772–781.
- Loaiza-Ganem, G.; Ross, B. L.; Hosseinzadeh, R.; Caterini, A. L.; and Cresswell, J. C. 2024. Deep Generative Models through the Lens of the Manifold Hypothesis: A Survey and New Connections. *Transactions on Machine Learning Research*.
- Lu, Z.; Huang, D.; Bai, L.; Qu, J.; Wu, C.; Liu, X.; and Ouyang, W. 2023. Seeing is not always believing: Benchmarking human and model perception of ai-generated images. *Advances in neural information processing systems*, 36: 25435–25447.
- Luo, C. 2022. Understanding diffusion models: A unified perspective. *arXiv preprint arXiv:2208.11970*.
- Luo, Y.; Du, J.; Yan, K.; and Ding, S. 2024. LaRE<sup>2</sup>: Latent reconstruction error based method for diffusion-generated image detection. In *Proceedings of the IEEE/CVF Conference on Computer Vision and Pattern Recognition*, 17006–17015.
- Ma, R.; Duan, J.; Kong, F.; Shi, X.; and Xu, K. 2024. Exposing the Fake: Effective Diffusion-Generated Images Detection. In *The Second Workshop on New Frontiers in Adversarial Machine Learning*.
- MidJourney. -. Midjourney. https://www.midjourney.com/home. [Accessed 31-07-2025].
- Nguyen-Le, H.-H.; Tran, V.-T.; Nguyen, D.-T.; and Le-Khac, N.-A. 2025. Deepfake Detection Across Image, Video, and Audio: A Comprehensive Survey with Empirical Evaluation of Generalization and Robustness.
- Ni, Y.; Meng, D.; Yu, C.; Quan, C.; Ren, D.; and Zhao, Y. 2022. Core: Consistent representation learning for face forgery detection. In *Proceedings of the IEEE/CVF Conference on Computer Vision and Pattern Recognition*, 12–21.
- Nichol, A.; Dhariwal, P.; Ramesh, A.; Shyam, P.; Mishkin, P.; McGrew, B.; Sutskever, I.; and Chen, M. 2021. Glide: Towards photorealistic image generation and editing with text-guided diffusion models. *arXiv preprint arXiv:2112.10741*.
- Nichol, A. Q.; and Dhariwal, P. 2021. Improved denoising diffusion probabilistic models. In *International conference on machine learning*, 8162–8171. PMLR.
- Ojha, U.; Li, Y.; and Lee, Y. J. 2023. Towards universal fake image detectors that generalize across generative models. In *Proceedings of the IEEE/CVF Conference on Computer Vision and Pattern Recognition*, 24480–24489.
- Pan, K.; Yin, Y.; Wei, Y.; Lin, F.; Ba, Z.; Liu, Z.; Wang, Z.; Cavallaro, L.; and Ren, K. 2023. Dfil: Deepfake incremental learning by exploiting domain-invariant forgery clues. In *Proceedings of the 31st ACM International Conference on Multimedia*, 8035–8046.

- Park, T.; Liu, M.-Y.; Wang, T.-C.; and Zhu, J.-Y. 2019. Semantic image synthesis with spatially-adaptive normalization. In *Proceedings of the IEEE/CVF conference on computer vision and pattern recognition*, 2337–2346.
- Patashnik, O.; Wu, Z.; Shechtman, E.; Cohen-Or, D.; and Lischinski, D. 2021. Styleclip: Text-driven manipulation of stylegan imagery. In *Proceedings of the IEEE/CVF international conference on computer vision*, 2085–2094.
- Peng, X.; Xiao, S.; Feng, J.; Yau, W.-Y.; and Yi, Z. 2016. Deep subspace clustering with sparsity prior. In *Proceedings of the Twenty-Fifth International Joint Conference on Artificial Intelligence*, 1925–1931.
- Qian, Q. 2023. Stable cluster discrimination for deep clustering. In *Proceedings of the IEEE/CVF international conference on computer vision*, 16645–16654.
- Radford, A.; Kim, J. W.; Hallacy, C.; Ramesh, A.; Goh, G.; Agarwal, S.; Sastry, G.; Askell, A.; Mishkin, P.; Clark, J.; et al. 2021. Learning transferable visual models from natural language supervision. In *International conference on machine learning*, 8748–8763. PmLR.
- Ramesh, A.; Dhariwal, P.; Nichol, A.; Chu, C.; and Chen, M. 2022. Hierarchical text-conditional image generation with clip latents. *arXiv preprint arXiv:2204.06125*, 1(2): 3.
- Rombach, R.; Blattmann, A.; Lorenz, D.; Esser, P.; and Ommer, B. 2022. High-resolution image synthesis with latent diffusion models. In *Proceedings of the IEEE/CVF conference on computer vision and pattern recognition*, 10684–10695.
- Shen, Y.; Shen, Z.; Wang, M.; Qin, J.; Torr, P.; and Shao, L. 2021. You never cluster alone. *Advances in Neural Information Processing Systems*, 34: 27734–27746.
- Shilin, Y.; Ouxiang, L.; Jiayin, C.; Yanbin, H.; Xiaolong, J.; Yao, H.; and Weidi, X. 2025. A Sanity Check for Algenerated Image Detection. In *The Thirteenth International Conference on Learning Representations*.
- Song, J.; Meng, C.; and Ermon, S. 2020. Denoising diffusion implicit models. *arXiv preprint arXiv:2010.02502*.
- Tan, C.; Zhao, Y.; Wei, S.; Gu, G.; Liu, P.; and Wei, Y. 2025. Rethinking the up-sampling operations in cnn-based generative network for generalizable deepfake detection. In *Proceedings of the IEEE/CVF Conference on Computer Vision and Pattern Recognition*, 28130–28139.
- Tan, C.; Zhao, Y.; Wei, S.; Gu, G.; and Wei, Y. 2023. Learning on gradients: Generalized artifacts representation for gan-generated images detection. In *Proceedings of the IEEE/CVF Conference on Computer Vision and Pattern Recognition*, 12105–12114.
- Tao, M.; Bao, B.-K.; Tang, H.; and Xu, C. 2023. Galip: Generative adversarial clips for text-to-image synthesis. In *Proceedings of the IEEE/CVF conference on computer vision and pattern recognition*, 14214–14223.
- Tao, M.; Tang, H.; Wu, F.; Jing, X.-Y.; Bao, B.-K.; and Xu, C. 2022. Df-gan: A simple and effective baseline for text-to-image synthesis. In *Proceedings of the IEEE/CVF conference on computer vision and pattern recognition*, 16515–16525.

- Tao, Y.; Takagi, K.; and Nakata, K. 2021. Clustering-friendly Representation Learning via Instance Discrimination and Feature Decorrelation. In *International Conference on Learning Representations*.
- Wang, S.-Y.; Wang, O.; Zhang, R.; Owens, A.; and Efros, A. A. 2020a. CNN-Generated Images Are Surprisingly Easy to Spot... for Now. In *Proceedings of the IEEE/CVF Conference on Computer Vision and Pattern Recognition (CVPR)*.
- Wang, S.-Y.; Wang, O.; Zhang, R.; Owens, A.; and Efros, A. A. 2020b. CNN-generated images are surprisingly easy to spot... for now. In *Proceedings of the IEEE/CVF conference on computer vision and pattern recognition*, 8695–8704.
- Wang, Z.; Bao, J.; Zhou, W.; Wang, W.; Hu, H.; Chen, H.; and Li, H. 2023. Dire for diffusion-generated image detection. In *Proceedings of the IEEE/CVF International Conference on Computer Vision*, 22445–22455.
- WhichFaceisReal. 2019. Which Face Is Real? which-faceisreal.com. https://www.whichfaceisreal.com/. [Accessed 23-07-2025].
- Wukong. 2022. Wukong. https://xihe.mindspore.cn/modelzoo/wukong. [Accessed 31-07-2025].
- Yan, S.; Li, O.; Cai, J.; Hao, Y.; Jiang, X.; Hu, Y.; and Xie, W. 2025a. A Sanity Check for AI-generated Image Detection. In *The Thirteenth International Conference on Learning Representations*.
- Yan, Z.; Wang, J.; Jin, P.; Zhang, K.-Y.; Liu, C.; Chen, S.; Yao, T.; Ding, S.; Wu, B.; and Yuan, L. 2025b. Orthogonal Subspace Decomposition for Generalizable AI-Generated Image Detection. *Forty-second International Conference on Machine Learning*.
- Yan, Z.; Yao, T.; Chen, S.; Zhao, Y.; Fu, X.; Zhu, J.; Luo, D.; Wang, C.; Ding, S.; Wu, Y.; et al. 2024. Df40: Toward next-generation deepfake detection. *Advances in Neural Information Processing Systems*, 37: 29387–29434.
- Yan, Z.; Zhang, Y.; Yuan, X.; Lyu, S.; and Wu, B. 2023. DeepfakeBench: A Comprehensive Benchmark of Deepfake Detection. *Advances in Neural Information Processing Systems*, 36: 4534–4565.
- Zhang, S.; You, C.; Vidal, R.; and Li, C.-G. 2021. Learning a self-expressive network for subspace clustering. In *Proceedings of the IEEE/CVF Conference on Computer Vision and Pattern Recognition*, 12393–12403.
- Zhang, X.; Karaman, S.; and Chang, S.-F. 2019. Detecting and simulating artifacts in gan fake images. In 2019 IEEE international workshop on information forensics and security (WIFS), 1–6. IEEE.
- Zhong, N.; Xu, Y.; Li, S.; Qian, Z.; and Zhang, X. 2023. Patchcraft: Exploring texture patch for efficient ai-generated image detection. *arXiv preprint arXiv:2311.12397*.
- Zhou, S.; Xu, H.; Zheng, Z.; Chen, J.; Li, Z.; Bu, J.; Wu, J.; Wang, X.; Zhu, W.; and Ester, M. 2024. A comprehensive survey on deep clustering: Taxonomy, challenges, and future directions. *ACM Computing Surveys*, 57(3): 1–38.

- Zhu, J.-Y.; Park, T.; Isola, P.; and Efros, A. A. 2017. Unpaired image-to-image translation using cycle-consistent adversarial networks. In *Proceedings of the IEEE international conference on computer vision*, 2223–2232.
- Zhu, M.; Chen, H.; Yan, Q.; Huang, X.; Lin, G.; Li, W.; Tu, Z.; Hu, H.; Hu, J.; and Wang, Y. 2023. Genimage: A million-scale benchmark for detecting ai-generated image. *Advances in Neural Information Processing Systems*, 36: 77771–77782.
- Zhuang, W.; Chu, Q.; Tan, Z.; Liu, Q.; Yuan, H.; Miao, C.; Luo, Z.; and Yu, N. 2022. UIA-ViT: Unsupervised inconsistency-aware method based on vision transformer for face forgery detection. In *European conference on computer vision*, 391–407. Springer.

## Appendix for Beyond Binary Classification: A Semi-supervised Approach to Generalized AI-generated Image Detection

#### **Proof of Theorem**

## **Key Definitions**

**Definition 1.** (GAN objective) Let  $\mathcal{D}$  and  $\mathcal{G}$  be the Discriminator and Generator of GAN, respectively. The GAN objective is defined by

$$\min_{\mathcal{C}} \max_{\mathcal{D}} V(\mathcal{D}, \mathcal{G}) = \mathbb{E}_{x \sim p_{\text{data}}}[\log(\mathcal{D}(x))] + \mathbb{E}_{z \sim p_z}[\log(1 - \mathcal{D}(\mathcal{G}(z)))], \tag{11}$$

where  $V(\mathcal{D}, \mathcal{G})$  represents the value function,  $p_z$  denotes the generator's distribution from which input vector z is sampled, and  $\mathcal{D}(\mathcal{G}(z))$  is the output of the Discriminator for a generated sample  $\mathcal{G}(z)$ .

**Definition 2.** (Diffusion Process) There are two processes in Diffusion Process, including the forward process and the reverse process:

1. The forward process is defined as:

$$q(x_t|x_{t-1}) = \mathcal{N}(x_t; \sqrt{1-\beta_t}x_{t-1}, \beta_t I) \qquad q(x_t|x_0) = \mathcal{N}(x_t; \sqrt{\tilde{\alpha}_t}x_0, (1-\tilde{\alpha}_t)I), \tag{12}$$

where  $\tilde{\alpha}_t = \prod_{s=1}^t \alpha_s$  and  $\alpha_t = 1 - \beta_t$ , with  $\beta \in (0,1)$  is a variance schedule.

2. The reverse process is defined as:

$$p_{\theta}(x_{0:T}) = p(x_T) \prod_{t=1}^{T} p_{\theta}(x_{t-1}|x_t) \qquad p_{\theta}(x_{t-1}|x_t) = \mathcal{N}(x_{t-1}; \mu_{\theta}(x_t, t), \Sigma_{\theta}(x_t, t)), \tag{13}$$

where  $\mu_{\theta}(x_t, t)$  is the mean of the reverse process distribution, which is predicted by a neural network with parameters  $\theta$ ,  $\Sigma_{\theta}(x_t, t)$  is the covariance matrix of the reverse process distribution, which is also learned, and  $\theta$  represents the learnable parameters of a neural network.

**Definition 3.** (Evidence Lower Bound) Let X, Y be random variables that have joint distribution  $p_{\theta}$ , and assume that  $x \sim p_{\text{data}}$  then Evidence Lower Bound, denoted ELBO, defined as:

$$ELBO(x) = \mathbb{E}_{y \sim q(\cdot|x)}[\log p_{\theta}(x, y) - \log q(y|x)], \tag{14}$$

where q is any distribution.

**Definition 4.** (Kullback-Leibler (KL) divergence) The KL divergence is a measure of how different two probability distributions are. Assum that p(x) is the true distribution and and q(x) is the approximate distribution. The Kullback-Leibler (KL) divergence defined by:

$$D_{KL}(P||Q) = \int p(x) \log\left(\frac{p(x)}{q(x)}\right) dx. \tag{15}$$

**Definition 5.** (Jensen-Shannon (JS) Divergence) Let P and Q be two probability distributions over the same probability space. The Jensen-Shannon Divergence is defined as:

$$D_{JS}(P||Q) = \frac{1}{2}D_{KL}(P||M) + \frac{1}{2}D_{KL}(Q||M), \tag{16}$$

where  $M = \frac{1}{2}(P+Q)$  is the mixture distribution of P and Q.

#### **Proof of Lemmas**

#### Lemma 1

*Proof.* From Definition 4, we have the KL divergence between  $p_{textdata}$  and  $p_{DM}$ :

$$D_{KL}(p_{\text{data}}||p_{DM}) = \int p_{\text{data}}(x_0) \log \left(\frac{p_{\text{data}}(x_0)}{p_{\text{DM}}(x_0)}\right) dx_0$$

$$= \int p_{\text{data}}(x_0) \log p_{\text{data}}(x_0) dx_0 - \int p_{\text{data}}(x_0) \log p_{\text{DM}}(x_0) dx_0$$

$$= \mathbb{E}_{x_0 \sim p_{\text{data}}}[\log p_{\text{data}}(x_0)] - \mathbb{E}_{x_0 \sim p_{\text{data}}}[\log p_{\text{DM}}(x_0)]$$

$$= -H(p_{\text{data}}) - \mathbb{E}_{\{x_0 \sim p_{\text{data}}\}}[\log p_{\text{DM}}(x_0)] \quad \text{(By Information Theory (Cover 1999))}$$

With  $p_{DM}(x_0)$ , Eq. 14 in Definition 3, for any distribution q, can be re-written as:

$$ELBO(x) = \mathbb{E}_{y \sim q(\cdot|x_0)} [\log p_{DM}(x_0, y) - \log q(y|x_0)]$$
(18)

Let  $y = x_{1:T}$  (the latent variables are the noisy versions of  $x_0$ ), and  $q(x_{1:T}|x_0)$  is the forward process from Definition 2. By the variational inference principle:

$$\log p_{\text{DM}}(x_{0}) = \log \int p_{\text{DM}}(x_{0}, x_{1:T}) dx_{1:T}$$

$$= \log \int q(x_{1:T}|x_{0}) \cdot \left[ \frac{p_{\text{DM}}(x_{0}, x_{1:T})}{q(x_{1:T}|x_{0})} \right] dx_{1:T}$$

$$\geq \int q(x_{1:T}|x_{0}) \log \left[ \frac{p_{\text{DM}}(x_{0}, x_{1:T})}{q(x_{1:T}|x_{0})} \right] dx_{1:T} \quad \text{(by Jensen's inequality)}$$

$$= \mathbb{E}_{x_{1:T} \sim q(\cdot|x_{0})} [\log p_{\text{DM}}(x_{0}, x_{1:T}) - \log q(x_{1:T}|x_{0})]$$

$$= \text{ELBO}(x_{0})$$
(19)

Therefore:

$$\log p_{\rm DM}(x_0) \ge \text{ELBO}(x_0) \tag{20}$$

which implies:

$$-\log p_{\rm DM}(x_0) \le -\text{ELBO}(x_0) \tag{21}$$

Substituting back into our expression for  $D_{KL}$ :

$$D_{KL}(p_{\text{data}}||p_{\text{DM}}) = -H(p_{\text{data}}) - \mathbb{E}_{\{x_0 \sim p_{\text{data}}\}}[\log p_{\text{DM}}(x_0)]$$

$$\leq -H(p_{\text{data}}) + \mathbb{E}_{\{x_0 \sim p_{\text{data}}\}}[-\text{ELBO}(x_0)]$$
(22)

Therefore, minimizing  $\mathbb{E}_{\{x_0 \sim p_{\text{data}}\}}[-\text{ELBO}(x_0)]$  provides an upper bound minimization for  $D_{\text{KL}}(p_{\text{data}}||p_{\text{DM}})$ .

#### Lemma 2

*Proof.* For a fixed generator  $\mathcal{G}$  and any discriminator  $\mathcal{D}$ , we have (from Definition 1):

$$V(\mathcal{D}, \mathcal{G}) = \mathbb{E}_{x \sim p_{\text{data}}}[\log(\mathcal{D}(x))] + \mathbb{E}_{z \sim p_z}[\log(1 - \mathcal{D}(\mathcal{G}(z)))]$$
(23)

Since  $\mathcal{G}(z)$  with  $z \sim p_z$  generates samples according to the distribution  $p_{\text{GAN}}$ , we can rewrite:

$$V(\mathcal{D}, \mathcal{G}) = \mathbb{E}_{x \sim p_{\text{data}}}[\log(\mathcal{D}(x))] + \mathbb{E}_{x \sim p_{\text{GAN}}}[\log(1 - \mathcal{D}(x))]$$
(24)

This can be expressed as an integral:

$$V(\mathcal{D}, \mathcal{G}) = \int p_{\text{data}}(x) \log(\mathcal{D}(x)) dx + \int p_{\text{GAN}}(x) \log(1 - \mathcal{D}(x)) dx$$

$$= \int [p_{\text{data}}(x) \log(\mathcal{D}(x)) + p_{\text{GAN}}(x) \log(1 - \mathcal{D}(x))] dx$$
(25)

For any fixed x, to maximize the integrated  $f(D(x)) = p_{data}(x) \log D(x) + p_{GAN}(x) \log(1 - D(x))$  with respect to  $\mathcal{D}(x) \in (0,1)$ , we take the derivative:

$$f'(\mathcal{D}) = \frac{p_{\text{data}}(x)}{\mathcal{D}} - \frac{p_{\text{GAN}}(x)}{1 - \mathcal{D}}$$
(26)

Setting  $f'(\mathcal{D}) = 0$  and solving:

$$\frac{p_{\text{data}}(x)}{\mathcal{D}(x)} = \frac{p_{\text{GAN}}(x)}{1 - \mathcal{D}(x)}$$

$$p_{\text{data}}(x)(1 - \mathcal{D}(x)) = p_{\text{GAN}}(x)\mathcal{D}(x)$$

$$p_{\text{data}}(x) = \mathcal{D}(x)(p_{\text{data}}(x) + p_{\text{GAN}}(x))$$
(27)

Therefore, the optimal discriminator:

$$\mathcal{D}^*(x) = \frac{p_{\text{data}}(x)}{p_{\text{data}}(x) + p_{\text{GAN}}(x)}$$
(28)

To verify this is a maximum, check the second derivative:

$$f''(\mathcal{D}) = -\frac{p_{\text{data}}(x)}{\mathcal{D}^2} - \frac{p_{\text{GAN}}(x)}{(1-\mathcal{D})^2} < 0$$

$$(29)$$

Since  $f''(\mathcal{D}) < 0$ ,  $\mathcal{D}$  gives the maximum value. As we know  $\mathcal{D}^*(x)$  maximizes the integrand for each x, we have for any discriminator  $\mathcal{D}$ :

$$p_{\text{data}}(x)\log D(x) + p_{\text{GAN}}(x)\log(1 - D(x)) \le p_{\text{data}}(x)\log D^*(x) + p_{\text{GAN}}(x)\log(1 - D^*(x))$$
(30)

Integrating over all x:

$$V(\mathcal{D}, \mathcal{G}) \le V(\mathcal{D}^*, \mathcal{G}),$$
 (31)

with equality if and only if  $\mathcal{D}(x) = \mathcal{D}^*(x)$  for almost all x.

Next, we substitute  $D^*(x)$  back into  $V(\mathcal{D}^*, \mathcal{G})$ :

$$V(\mathcal{D}^*, \mathcal{G}) = \mathbb{E}_{x \sim p_{\text{data}}} \left[ \log \frac{p_{\text{data}}(x)}{p_{\text{data}}(x) + p_{\text{GAN}}(x)} \right] + \mathbb{E}_{x \sim p_{\text{GAN}}} \left[ \log \frac{p_{\text{GAN}}(x)}{p_{\text{data}}(x) + p_{\text{GAN}}(x)} \right]$$
(32)

Recall from Definition 5, for our case, let  $M = \frac{1}{2}(p_{data} + p_{GAN})$ . Then:

$$D_{JS}(p_{\text{data}} || p_{\text{GAN}}) = \frac{1}{2} D_{KL}(p_{\text{data}} || M) + \frac{1}{2} D_{KL}(p_{\text{GAN}} || M)$$

$$= \frac{1}{2} \mathbb{E}_{x \sim p_{\text{data}}} \left[ \log \frac{p_{\text{data}}(x)}{M(x)} \right] + \frac{1}{2} \mathbb{E}_{x \sim p_{\text{GAN}}} \left[ \log \frac{p_{\text{GAN}}(x)}{M(x)} \right]$$

$$= \frac{1}{2} \mathbb{E}_{x \sim p_{\text{data}}} \left[ \log \frac{2p_{\text{data}}(x)}{p_{\text{data}}(x) + p_{\text{GAN}}(x)} \right] + \frac{1}{2} \mathbb{E}_{x \sim p_{\text{GAN}}} \left[ \log \frac{2p_{\text{GAN}}(x)}{p_{\text{data}}(x) + p_{\text{GAN}}(x)} \right]$$
(33)

Using the property  $\log(2a) = \log 2 + \log a$ :

$$D_{JS}(p_{\text{data}} || p_{\text{GAN}}) = \frac{1}{2} \log 2 + \frac{1}{2} \mathbb{E}_{x \sim p_{\text{data}}} \left[ \log \frac{p_{\text{data}}(x)}{p_{\text{data}}(x) + p_{\text{GAN}}(x)} \right]$$

$$+ \frac{1}{2} \log 2 + \frac{1}{2} \mathbb{E}_{x \sim p_{\text{GAN}}} \left[ \log \frac{p_{\text{GAN}}(x)}{p_{\text{data}}(x) + p_{\text{GAN}}(x)} \right]$$

$$= \log 2 + \frac{1}{2} V(\mathcal{D}^*, \mathcal{G})$$
(34)

Rearranging, we have:

$$V(\mathcal{D}^*, \mathcal{G}) = 2D_{JS}(p_{\text{data}} || p_{\text{GAN}}) - 2\log 2$$

$$\tag{35}$$

Combining Eq. 31 and 35, we have:

$$V(\mathcal{D}, \mathcal{G}) \le V(\mathcal{D}^*, \mathcal{G} = 2D_{JS}(p_{\text{data}}||p_{\text{GAN}}) - 2\log 2$$
(36)

#### **Complete Proof of Theorem 1**

**Proof. Part 1: GAN Optimization:** 

From Lemma 2, we established that for a fixed generator  $\mathcal{G}$ , the value function satisfies:

$$V(\mathcal{D}, \mathcal{G}) \le 2D_{JS}(p_{\text{data}} || p_{\text{GAN}}) - 2\log 2 \tag{37}$$

When the discriminator is optimal, we have:

$$V(\mathcal{D}^*, \mathcal{G}) = 2D_{\text{JS}}(p_{\text{data}} || p_{\text{GAN}}) - 2\log 2$$
(38)

The GAN training objective for the generator is is to minimize the value function with respect to  $\mathcal{G}$ :

$$\min_{\mathcal{G}} V(\mathcal{D}^*, \mathcal{G}) = \min_{\mathcal{G}} [2D_{JS}(p_{\text{data}} || p_{\text{GAN}}) - 2\log 2]$$

Since  $-2 \log 2$  is a constant independent of  $\mathcal{G}$ , minimizing  $V(\mathcal{D}^*, \mathcal{G})$  is equivalent to minimizing  $D_{JS}(p_{\text{data}}|p_{\text{GAN}})$ :

$$\min_{\mathcal{G}} V(\mathcal{D}^*, \mathcal{G}) \equiv \min D_{\text{JS}}(p_{\text{data}} || p_{\text{GAN}})$$
(39)

Therefore, GANs minimize the JS divergence between the data distribution and the generated distribution.

## Part 2: DM Optimization:

From Lemma 1, we established that DMs minimize an upper bound on the KL divergence:

$$D_{KL}(p_{\text{data}}||p_{\text{DM}}) \le \mathbb{E}_{\{x_0 \sim p_{\text{data}}\}}[-\text{ELBO}(x_0)] + H(p_{\text{data}}) \tag{40}$$

The DM training objective is to maximize the ELBO, which is equivalent to minimizing -ELBO:

$$\min_{a} \mathbb{E}_{x_0 \sim p_{\text{data}}} [-\text{ELBO}(x_0)], \tag{41}$$

where  $\theta$  represents the parameters of the reverse process.

From Remark 1, the inequality becomes an equality when the variational posterior  $q(x_{1:T}|x_0)$  (the forward process) matches the true posterior  $p_{\theta}(x_{1:T}|x_0)$  under the model. At the global optimum with sufficient model capacity:

$$D_{KL}(p_{\text{data}}||p_{\text{DM}}) = \mathbb{E}_{x_0 \sim p_{\text{data}}}[-\text{ELBO}(x_0)] + H(p_{\text{data}})$$

Since  $H(p_{\text{data}})$  is a constant (independent of model parameters), minimizing the right-hand side is equivalent to minimizing:

$$\min_{\theta} \mathbb{E}_{x \sim p_{\text{data}}}[-\text{ELBO}(x)] \equiv \min_{\theta} D_{KL}(p_{\text{data}} || p_{\text{DM}})$$
(42)

### **Complete Proof of Theorem 2**

We assume all distributions admit densities with respect to a common base measure  $\mu$  on  $\mathcal{X}$ . For notational convenience, we use the same symbols for distributions and their densities.

*Proof.* Part 1: GANs Support Analysis. From Definition 5, the JS divergence between  $p_{data}$  and  $p_{GAN}$  is defined as:

$$D_{JS}(p_{\text{data}}||p_{\text{GAN}}) = \frac{1}{2}D_{KL}(p_{\text{data}}||M) + \frac{1}{2}D_{KL}(p_{\text{GAN}}||M)$$

$$= \frac{1}{2}\int \underbrace{p_{\text{data}}(x)\log\left(\frac{p_{\text{data}}(x)}{M(x)}\right)dx}_{(*)} + \frac{1}{2}\int \underbrace{p_{\text{GAN}}(x)\log\left(\frac{p_{\text{GAN}}(x)}{M(x)}\right)dx}_{(**)}$$

$$\tag{43}$$

where  $M = \frac{1}{2}(p_{\text{data}} + p_{\text{GAN}})$  is the mixture distribution.

Let us analyze the first integral for any  $x \in S_{\text{data}}$  (where  $p_{\text{data}}(x) > 0$ ):

• Case 1: If  $p_{GAN}(x) = 0$ , then  $M(x) = \frac{1}{2}p_{data}(x) > 0$ . The contribution to the first term (\*) at point x is:

$$\lim_{p_{\text{GAN}}(x) \to 0} p_{\text{data}}(x) \log \left( \frac{p_{\text{data}}(x)}{M(x)} \right) = p_{\text{data}}(x) \log \left( \frac{p_{\text{data}}(x)}{\frac{1}{2} p_{\text{data}}(x)} \right) = p_{\text{data}}(x) \log 2$$
(44)

Since  $\log 2$  is finite, the integral of the first term (\*)  $\int p_{\text{data}}(x) \log \left( \frac{p_{\text{data}}(x)}{M(x)} \right) < 0$  remains finite even when  $S_{\text{GAN}} \subset S_{\text{data}}$ .

• Case 2: If  $p_{\text{GAN}}(x) > 0$ , then  $M(x) = \frac{1}{2}(p_{\text{data}} + p_{\text{GAN}}) > 0$  and the integral of the first term (\*) is finite. For the second KL term (\*\*), we only integrate over  $x : p_{GAN}(x) > 0$ . Since  $p_{GAN}(x) > 0 \implies M(x) \ge \frac{1}{2}p_{GAN}(x) > 0$ , this integral is well-defined and finite. Therefore:

$$D_{JS}(p_{data}||p_{GAN}) = \frac{1}{2}D_{KL}(p_{data}||M) + \frac{1}{2}D_{KL}(p_{GAN}||M) < \infty$$
(45)

The JS divergence remains finite even when  $S_{GAN} \subset S_{data}$ , allowing GANs to achieve optimal solutions without full support coverage.

## Part 2: DMs Support Analysis

From Lemma 1, DMs minimize:

$$D_{KL}(p_{\text{data}}||p_{\text{DM}}) = \int p_{\text{data}}(x) \log \left(\frac{p_{\text{data}}(x)}{p_{\text{DM}}(x)}\right) dx \tag{46}$$

Suppose there exists a set  $A \subseteq S_{\text{data}}$  with positive measure under  $p_{\text{data}}$  such that  $p_{\text{DM}}(x) = 0$  for all  $x \in A$ . We can decompose the integral:

$$D_{KL}(p_{\text{data}}|p_{\text{DM}}) = \underbrace{\int_{\mathcal{A}} p_{\text{data}}(x) \log \left(\frac{p_{\text{data}}(x)}{p_{\text{DM}}(x)}\right) dx}_{\text{Problematic part: } p_{\text{DM}}(x) = 0} + \underbrace{\int_{\mathcal{S}_{\text{data}} \setminus \mathcal{A}} p_{\text{data}}(x) \log \left(\frac{p_{\text{data}}(x)}{p_{\text{DM}}(x)}\right) dx}_{\text{Well-behaved part: } p_{\text{DM}}(x) > 0}$$
(47)

For any  $x \in \mathcal{A}$ , we have  $p_{\text{data}}(x) > 0$  (since  $x \in \mathcal{S}$ data) and pDM(x) = 0. To evaluate the integral over  $\mathcal{A}$ , we consider the limit:

$$\lim_{p_{\mathrm{DM}}(x)\to 0^{+}} p_{\mathrm{data}}(x) \log \left(\frac{p_{\mathrm{data}}(x)}{p_{\mathrm{DM}}(x)}\right) = p_{\mathrm{data}}(x) \cdot \lim_{p_{\mathrm{DM}}(x)\to 0^{+}} \log \left(\frac{p_{\mathrm{data}}(x)}{p_{\mathrm{DM}}(x)}\right) = +\infty \tag{48}$$

Since  $p_{\text{data}}(x) > 0$  is fixed and  $\lim_{p_{\text{DM}}(x) \to 0^+} \log \left( \frac{p_{\text{data}}(x)}{p_{\text{DM}}(x)} \right) = +\infty$ .

Therefore:

$$\int_{A} p_{\text{data}}(x) \log \left( \frac{p_{\text{data}}(x)}{p_{\text{DM}}(x)} \right) dx = +\infty$$
(49)

This implies:

$$D_{\rm KL}(p_{\rm data}||p_{\rm DM}) = +\infty \tag{50}$$

Since the optimization objective is to minimize  $D_{\text{KL}}(p_{\text{data}}||p_{\text{DM}})$ , any distribution  $p_{\text{DM}}$  with  $S_{\text{DM}} \not\supseteq S_{\text{data}}$  yields an infinite objective value and cannot be optimal. For DMs to achieve a finite (and thus optimizable) KL divergence, we must have  $S_{\text{data}} \subseteq S_{\text{DM}}$ .

## Sinkhorn-Knopp Algorithm

### Algorithm 2: Sinkhorn-Knopp Algorithm

```
Require: Logits s^{\text{fake}} \in \mathbb{R}^{B \times K}, temperature \epsilon, iterations TEnsure: Balanced assignment matrix Q \in \mathbb{R}^{B \times K}1: Q^{(0)} \leftarrow \exp(s^{\text{fake}}/\epsilon)> Initialize with softmax2: for t = 1 to T do> Row normalization3: Q^{(t)} \leftarrow \mathcal{R}(Q^{(t-1)})> Row normalization4: Q^{(t)} \leftarrow \mathcal{C}(Q^{(t)})> Column normalization5: end for6: Q \leftarrow \mathcal{R}(Q^{(T)})> Final row normalization7: return Q
```

## **Experimental Details**

#### **Datasets**

We evaluate TriDetect on 2 standard benchmarks (GenImage (Zhu et al. 2023), AIGCDetectBenchmark (Zhong et al. 2023)) and 3 in-the-wild datasets (WildFake (Hong et al. 2025), Chameleon (Shilin et al. 2025), DF40 (Yan et al. 2024)):

- GenImage (Zhu et al. 2023): GenImage includes 331,167 real images and 1,350,000 AI-generated images. Synthetic images generated by generators: Midjourney (MidJourney –), SD (V1.4 and V1.5) (Rombach et al. 2022), ADM (Dhariwal and Nichol 2021), GLIDE (Nichol et al. 2021), Wukong (Wukong 2022), VQDM (Gu et al. 2022), and BigGAN (Brock, Donahue, and Simonyan 2018).
- AIGCDetectBenchmark (Zhong et al. 2023): This dataset includes synthetic images created by 16 generators: ProGAN (Karras et al. 2017), StyleGAN (Karras, Laine, and Aila 2019), BigGAN (Brock, Donahue, and Simonyan 2018), CycleGAN (Zhu et al. 2017), StarGAN (Choi et al. 2018), GauGAN (Park et al. 2019), Stylegan2 (Karras et al. 2020), ADM (Dhariwal and Nichol 2021), Glide GLIDE (Nichol et al. 2021), VQDM (Gu et al. 2022), Wukong (Wukong 2022), Midjourney (MidJourney –), Stable Diffusion (SDv1.4, SDv1.5) (Rombach et al. 2022), DALL-E 2 (Ramesh et al. 2022), and SD\_XL (Rombach et al. 2022).
- WildFake (Hong et al. 2025): Testing sets in this dataset applied by a series of degradation techniques: downsampling, JPEG compression, geometric transformations (flipping, cropping), adding watermarks (textual or visual), and color transformations. We evaluate TriDetect on these generators: DALL-E (Ramesh et al. 2022), DDPM (Nichol and Dhariwal 2021), DDIM (Song, Meng, and Ermon 2020), VQDM (Gu et al. 2022), BigGAN (Brock, Donahue, and Simonyan 2018), StarGAN (Choi et al. 2018), StyleGAN (Karras, Laine, and Aila 2019), DF-GAN (Tao et al. 2022), GALIP (Tao et al. 2023), GigaGAN (Kang et al. 2023).
- DF40 (Yan et al. 2024): DF40 contains more than 40 GAN-based and DM-based generators. In our work, we select 7 generators for evaluation: CollabDiff (Huang et al. 2023), MidJourney (MidJourney –), DeepFaceLab (DeepFaceLab –), StarGAN (Choi et al. 2018), StarGAN2 (Choi et al. 2020), StyleCLIP (Patashnik et al. 2021), and WhichisReal (WhichFaceisReal 2019).
- Chameleon (Shilin et al. 2025): Synthetic images in this dataset are designed to be challenging for human perception. The dataset contains approximately 26,000 test images in total, without separated into different generator subsets.

## **Implementation**

Our implementation employs a pre-trained CLIP ViT-L/14 vision encoder (f) with 1024-dimensional output features, then fine-tuned using Low-Rank Adaptation (LoRA) with rank r=16 and scaling factor  $\alpha=32$ , applied exclusively to the query and key projection matrices. The architecture-aware classifier consists of a three-layer MLP classifier  $g_{\theta}: \mathbb{R}^{1024} \to \mathbb{R}^3$  with hidden dimensions [256, 128] and ReLU activations, producing logits for one real class and two fake clusters. The Sinkhorn-Knopp algorithm operates with temperature  $\epsilon=0.05$  and T=3 iterations, ensuring balanced cluster assignments where each cluster receives approximately B/K samples.

For training stability, we compute binary logits using the numerically stable log-sum-exp formulation:  $Z_{\text{real}} = z_0$  and  $Z_{\text{fake}} = \log(\exp(z_1) + \exp(z_2))$ . The cross-prediction loss is implemented by computing balanced assignments  $Q = \text{Sinkhorn}(Z_{\text{fake}})$  and  $Q' = \text{Sinkhorn}(Z'_{\text{fake}})$  for original and augmented views respectively, then optimizing  $\mathcal{L}\text{cross} = -\frac{1}{2}[\sum_i Q' i \log p_i + \sum_i Q_i \log p' i]$  with detached assignments to prevent trivial solutions.

We use Adam optimizer with learning rate  $\eta=2\times 10^{-4}$ ,  $(\beta_1,\beta_2)=(0.9,0.95)$ , and weight decay  $\lambda=10^{-4}$ . The total loss combines binary classification and clustering objectives with weights  $\mathcal{L}_{\text{total}}=0.7\mathcal{L}_{\text{binary}}+0.3\mathcal{L}_{\text{cluster}}$ , where the cluster loss includes cross-prediction ( $\omega_1=1.0$ ) and cross-view consistency ( $\omega_2=0.1$ ) terms. Training is conducted with batch size B=128 for 5 epochs on randomly shuffled GAN and diffusion-generated images. CLIP-specific normalization is applied to  $224\times 224$  input images, where each RGB channel is normalized as  $x'=\frac{x-\mu}{\sigma}$  with per-channel means  $\mu=[0.481,\,0.458,\,0.408]$  and standard deviations  $\sigma=[0.269,\,0.261,\,0.276]$ .

For CNNSpot (Wang et al. 2020b), LNP (Liu et al. 2022), FreDect (Frank et al. 2020), Fusing (Ju et al. 2022), LGrad (Tan et al. 2023), DIRE (Wang et al. 2023), UnivFD (Ojha, Li, and Lee 2023), AIDE (Shilin et al. 2025) baselines, we utilize the implementation provided by AIGCDetectBenchmark (Zhong et al. 2023) for implementation. Regarding CORE (Ni et al. 2022), SPSL (Liu et al. 2021), UIA-VIT (Zhuang et al. 2022) and Effort (Yan et al. 2025b), we use the implementation provided by DeepfakeBench (Yan et al. 2023). Excluding from NPR (Tan et al. 2025), we use the official source code provided by the authors.

All experiments are conducted using a single run with a fixed random seed of 1024. To ensure robust evaluation despite using a single run, we compensate by evaluating each method across multiple diverse benchmarks. Our computational environment consists of an NVIDIA H100 NVL GPU with 94GB of VRAM, 48 CPU cores on a Linux operating system. The implementation is based on PyTorch 2.3.1 with Python 3.9.

	AUC	ACC	EER	AP
Cross-entropy loss	0.7265	0.5963	0.3411	0.6493
ArcFace loss (Deng et al. 2019)	0.7616	0.6104	0.3007	0.7017
Ours	0.8935	0.6788	0.1843	0.8742

Table 8: Performance evaluation on Chameleon dataset with existing attribution baselines.

Table 9: Ablation studies on different numbers of fake clusters. Results are evaluated on Chameleon dataset.

Number of fake clusters	AUC	ACC	EER	AP
2	0.8935	0.6788	0.1843	0.8742
3	0.8191	0.5978	0.2538	0.7847
4	0.8211	0.5867	0.2518	0.7756
5	0.7396	0.5911	0.3246	0.6979

#### **Additional Ablations and Results**

In this section, we provide additional experimental results and ablation studies of our proposed method.

#### **Comparison with Attribution Baselines**

Table 8 presents a comparison between our semi-supervised detection approach and existing attribution baselines. It is important to emphasize that our method is not designed for the attribution task, which identifies which specific generator produced a fake image. Instead, our approach focuses on discovering latent architectural patterns to enhance binary detection performance. Despite this fundamental difference in objectives, we include this comparison to demonstrate the effectiveness of our approach. The results reveal that our method substantially outperforms both attribution baselines, showing that discovering and leveraging architectural patterns through semi-supervised learning is effective for generalized detection.

## **Ablation Study on Different Number of Fake Clusters**

Table 9 demonstrates that the optimal number of fake clusters is K=2, which achieves the best performance across all metrics with an AUC of 0.8935 and the lowest EER of 0.1843. This result strongly aligns with our objective of having the model discover distinct architectural patterns that separate GAN-generated images from those created by diffusion models in the feature space.

## **Experimental Results on Standard Benchmarks and In-the-wild Datasets**

In our manuscript, we mainly present the AUC results on GenImage (Zhu et al. 2023) and AIGCDetectBenchmark (Zhong et al. 2023) datasets. This section reports the evaluation results on these two datasets across 3 metrics: ACC, EER, and AP. On GenImage (Tables 10-12), TriDetect achieves an average ACC of 0.9111, the lowest EER of 0.0343, and the average precision of 0.9894. On AIGCBenchmark (Tables 13-15), TriDetect also outperforms SoTA methods.

Regarding challenging real-world datasets: WildFake (Hong et al. 2025) and DF40 (Yan et al. 2024), only ACC results are reported in the main manuscript. In this section, tables 3-21 demonstrate TriDetect's generalization capability across other metrics: AUC, EER, and AP. Although degradation techniques are applied to testing sets of WildFake, our method shows higher results than other methods across all metrics. This demonstrates the better robustness of TriDetect than other methods.

Table 10: Comparison on the GenImage (Zhu et al. 2023) Dataset in terms of ACC Performance. The best result and the second-best result are marked in **bold** and underline, respectively.

Method	BigGAN	SD v1.4	ADM	GLIDE	MidJourney	VQDM	Wukong	Avg
CNNSpot	0.9988	0.9910	0.5170	0.5882	0.5344	0.5106	0.9658	0.7294
FreDect	0.9853	0.9720	0.5368	0.5533	0.5473	0.6113	0.9443	0.7358
Fusing	0.9988	0.9948	0.5081	0.5664	0.5098	0.5317	0.9718	0.7259
LGrad	0.6037	0.5308	0.5181	0.6103	0.5301	0.5181	0.5588	0.5528
LNP	0.9138	0.9178	0.5056	0.6089	0.5362	0.5398	0.8878	0.7014
CORE	0.9986	0.9933	0.5683	0.9498	0.5299	0.5580	0.9643	0.7946
SPSL	0.9940	0.9313	0.5008	0.5358	0.5292	0.5192	0.8925	0.7004
UIA-ViT	0.9965	0.9860	0.5038	0.7339	0.5768	0.5452	0.9322	0.7535
DIRE	0.9923	0.9943	0.5988	0.8976	0.6320	0.6056	0.9713	0.8131
UnivFD	0.9833	0.9653	0.7212	0.9482	0.7583	0.9143	0.8569	0.8696
AIDE	0.9813	0.9508	0.5637	0.7567	0.7174	0.6528	0.8972	0.7885
NPR	0.9918	0.9792	0.7745	0.7751	0.7748	0.8078	0.9177	0.8601
Effort	0.9991	0.9993	0.5872	0.7942	0.7411	0.9194	0.9878	0.8612
TriDetect	0.9991	0.9993	0.7482	0.9488	0.7180	0.9679	0.9963	0.9111

Table 11: Comparison on the GenImage (Zhu et al. 2023) Dataset in terms of EER Performance. The best result and the second-best result are marked in **bold** and underline, respectively.

Method	BigGAN	SD v1.4	ADM	GLIDE	MidJourney	VQDM	Wukong	Avg
CNNSpot	0.0007	0.0052	0.2593	0.1050	0.2815	0.2747	0.0153	0.1345
FreDect	0.0008	0.0275	0.3145	0.3017	0.3275	0.2697	0.0525	0.1849
Fusing	0.0007	0.0045	0.3152	0.1183	0.3637	0.2898	0.0128	0.1579
LGrad	0.4022	0.4673	0.4823	0.3818	0.4613	0.4827	0.4337	0.4445
LNP	0.0703	0.0693	0.4257	0.2360	0.3890	0.3683	0.0923	0.2359
CORE	0.0005	0.0050	0.2568	0.0273	0.2628	0.2570	0.0202	0.1185
SPSL	0.0055	0.0267	0.4323	0.2482	0.3167	0.2935	0.0430	0.1951
UIA-ViT	0.0030	0.0117	0.3313	0.1227	0.2813	0.2822	0.0348	0.1524
DIRE	0.0073	0.0053	0.2518	0.0632	0.2383	0.2542	0.0253	0.1208
UnivFD	0.0162	0.0317	0.1527	0.0433	0.1528	0.0593	0.0922	0.0783
AIDE	0.0050	0.0493	0.2968	0.1463	0.2127	0.2067	0.0882	0.1436
NPR	0.0052	0.0183	0.1462	0.0260	0.1302	0.1105	0.0610	0.0710
Effort	0.0002	0.0007	0.1763	0.0520	0.0768	0.0253	0.0067	0.0483
TriDetect	0.0005	0.0007	0.1032	0.0087	0.1133	0.0110	0.0030	0.0343

Table 12: Comparison on the GenImage (Zhu et al. 2023) Dataset in terms of AP Performance. The best result and the second-best result are marked in **bold** and underline, respectively.

Method	BigGAN	SD v1.4	ADM	GLIDE	MidJourney	VQDM	Wukong	Avg
CNNSpot	1.0000	0.9999	0.8075	0.9518	0.8025	0.7847	0.9989	0.9064
FreDect	1.0000	0.9971	0.7140	0.7391	0.7193	0.8049	0.9902	0.8521
Fusing	0.9999	0.9999	0.7287	0.9333	0.6845	0.7767	0.9987	0.8745
LGrad	0.6380	0.5928	0.5157	0.6205	0.5417	0.5136	0.6337	0.5794
LNP	0.9801	0.9818	0.5653	0.8123	0.6393	0.6597	0.9688	0.8010
CORE	1.0000	0.9998	0.8330	0.9960	0.8189	0.8272	0.9975	0.9246
SPSL	0.9998	0.9971	0.5762	0.8188	0.7562	0.7588	0.9924	0.8427
UIA-ViT	1.0000	0.9993	0.6704	0.9538	0.8145	0.7873	0.9949	0.8886
DIRE	0.9997	0.9997	0.8315	0.9854	0.8542	0.8362	0.9968	0.9291
UnivFD	0.9988	0.9954	0.9203	0.9915	0.9275	0.9854	0.9685	0.9696
AIDE	0.9998	0.9897	0.7298	0.9149	0.8706	0.8479	0.9715	0.9035
NPR	0.9999	0.9980	0.9427	0.9964	0.9479	0.9593	0.9874	0.9759
Effort	1.0000	1.0000	0.9088	0.9896	0.9803	0.9971	0.9998	0.9822
TriDetect	1.0000	1.0000	0.9656	0.9992	0.9616	0.9992	0.9999	0.9894

Table 13: Comparison on the AIGCDetectBenchmark (Zhong et al. 2023) Dataset in terms of ACC Performance. The best result and the second-best result are marked in **bold** and underline, respectively.

Poppor	Crow CAA	$s_{\mathcal{W}eG_{4N}}$	Specarz	Procedy	Gauc <sub>AA</sub>	Starcedy	BigGAN	MOP	Wakong	Clide	a ag	MOOA	MidJourney	80 V.4	\$1 <sub>1</sub> 0 <sub>8</sub>	DALLEZ	A. S.
CNNSpot	0.4974	0.5102	0.5029	0.4975	0.5027	0.5000	0.4858	0.5170	0.9658	0.5882	0.5200	0.5106	0.5344	0.9910	0.9903	0.5810	0.6059
FreDect	0.5049	0.5645	0.5538	0.5405	0.5330	0.5720	0.7083	0.5368	0.9443	0.5533	0.6273	0.6113	0.5473	0.9720	0.9723	0.5530	0.6434
Fusing	0.4890	0.5034	0.4991	0.5013	0.5022	0.4950	0.4978	0.5081	0.9718	0.5664	0.5163	0.5318	0.5098	0.9948	0.9928	0.5310	0.6007
LGrad	0.4837	0.4819	0.4383	0.4970	0.4644	0.4985	0.4985	0.5169	0.5593	0.6264	0.4643	0.5078	0.5242	0.5346	0.5347	0.5885	0.5137
LNP	0.4720	0.5000	0.4955	0.5000	0.4973	0.4855	0.4928	0.5059	0.8882	0.6103	0.5385	0.5398	0.5366	0.9177	0.9176	0.5570	0.5909
CORE	0.5061	0.5094	0.5003	0.5083	0.5027	0.6153	0.5063	0.5684	0.9643	0.9498	0.5093	0.5581	0.5298	0.9933	0.9921	0.5920	0.6441
SPSL	0.5091	0.4984	0.4970	0.5025	0.4999	0.4957	0.5093	0.5008	0.8925	0.5358	0.5180	0.5192	0.5292	0.9313	0.9296	0.5275	0.5872
UIA-ViT	0.5220	0.5187	0.5225	0.4974	0.4989	0.5230	0.5228	0.5038	0.9322	0.7339	0.6313	0.5452	0.5768	0.9860	0.9851	0.5655	0.6291
DIRE	0.5140	0.5495	0.5597	0.6496	0.4944	0.6601	0.5330	0.5985	0.9713	0.8973	0.6170	0.6055	0.6320	0.9943	0.9919	0.7605	0.6893
UnivFD	0.8812	0.6551	0.6696	0.7349	0.9359	0.7691	0.8273	0.7212	0.8469	0.9482	0.8145	0.9143	0.7583	0.9653	0.9650	0.8715	0.8299
AIDE	0.5473	0.6143	0.5933	0.7096	0.6633	0.5768	0.6613	0.5637	0.8972	0.7567	0.7510	0.6528	0.7174	0.9508	0.9499	0.7190	0.7078
NPR	0.7354	0.8438	0.8496	0.8986	0.5058	0.9927	0.6993	0.7745	0.9177	0.9751	0.8600	0.8078	0.7748	0.9792	0.9774	0.9635	0.8472
Effort	0.9387	0.8625	0.8201	0.9020	0.9874	0.9250	0.9863	0.5872	0.9878	0.7942	0.8838	0.9194	0.7411	0.9993	0.9985	0.7525	0.8804
TriDetect	0.9974	0.8654	0.7702	0.9909	0.9807	0.9230	0.9760	0.7482	0.9963	0.9488	0.7915	0.9679	0.7480	0.9993	0.9986	0.9405	0.9152

## **Limitation and Future Work**

In our manuscript and supplementary, we have provided detailed proofs for our theoretical analysis and conducted comprehensive experimental results and ablation studies to validate our proposed method - TriDetect. Results show that by discovering latent clusters within synthetic images that correspond to different generative architectures, TriDetect can improve the generalization capabilities to unseen generators across 5 datasets. One limitation of our work is that our method can generalize to unseen generators within the same architecture families as GANs and DMs, potentially failing to detect synthetic images generated by other architectures (e.g., VAE, normalizing flows).

In the future, we plan to extend our method into *open-set recognition* settings where the model can not only detect known architectural patterns but also identify and flag images from entirely novel generation paradigms. This would involve developing an outlier detection mechanism that monitors the distance between test samples and learned cluster centroids, enabling the system to recognize when an image exhibits patterns inconsistent with both real images and known synthetic architectures. Another promising direction is the development of *adaptive clustering mechanisms* that can dynamically adjust the number of clusters based on the observed data distribution.

Table 14: Comparison on the AIGCDetectBenchmark (Zhong et al. 2023) Dataset in terms of EER Performance. The best result and the second-best result are marked in **bold** and underline, respectively.

Mehod	Grecan	$s_{0}$ e $c_{4N}$	SyleGAN2	ProGAN	Gauc <sub>AA</sub>	StarGAN	BigGAN	MOP	Wakong	Clide	H ag	Mada	MidJourney	80 v.4	\$p_12	PALLEZ	₹ <u>*</u>
CNNSpot	0.6109	0.4782	0.5159	0.4923	0.5556	0.4562	0.5760	0.2595	0.0153	0.1048	0.2555	0.2747	0.2815	0.0052	0.0063	0.0740	0.3101
FreDect	0.5783	0.3893	0.3708	0.3425	0.4466	0.3382	0.2615	0.3145	0.0525	0.3017	0.2040	0.2697	0.3275	0.0275	0.0279	0.2530	0.2816
Fusing	0.5950	0.4877	0.4735	0.5190	0.5150	0.4912	0.5925	0.3150	0.0130	0.1185	0.2925	0.2898	0.3637	0.0045	0.0063	0.0970	0.3234
LGrad	0.5185	0.5196	0.5628	0.4998	0.5326	0.5063	0.5040	0.4830	0.4373	0.3683	0.5375	0.4912	0.4705	0.4642	0.4614	0.4130	0.5909
LNP	0.5731	0.4921	0.5091	0.5008	0.5068	0.5528	0.5490	0.4257	0.0920	0.2358	0.3415	0.3695	0.3880	0.0702	0.0713	0.2470	0.3703
CORE	0.4232	0.4260	0.4384	0.4560	0.4814	0.0860	0.4590	0.2562	0.0203	0.0273	0.3045	0.2570	0.2627	0.0050	0.0066	0.1070	0.2510
SPSL	0.4391	0.4754	0.4772	0.4813	0.4840	0.4782	0.3905	0.4323	0.0430	0.2482	0.2485	0.2935	0.3167	0.0267	0.0298	0.2370	0.3188
UIA-ViT	0.4981	0.3475	0.3065	0.4970	0.5086	0.4957	0.3905	0.3313	0.0348	0.1227	0.1375	0.2822	0.2813	0.0117	0.0134	0.2610	0.2825
DIRE	0.4164	0.4225	0.4007	0.2790	0.5722	0.0360	0.4655	0.2517	0.0255	0.0632	0.1890	0.2540	0.2383	0.0053	0.0075	0.1010	0.2330
UnivFD	0.0984	0.3402	0.3294	0.1270	0.0630	0.1536	0.0895	0.1527	0.0922	0.0433	0.1045	0.0593	0.1528	0.0317	0.0324	0.0970	0.1229
AIDE	0.4164	0.3372	0.3400	0.2735	0.2330	0.3507	0.2575	0.2968	0.0882	0.1463	0.1425	0.2067	0.2127	0.0493	0.0491	0.1880	0.2242
NPR	0.1499	0.1751	0.1383	0.1028	0.4756	0.0040	0.2865	0.1462	0.0610	0.0260	0.0840	0.1105	0.1302	0.0183	0.0216	0.0370	0.1229
Effort	0.0507	0.1349	0.1852	0.0238	0.0090	0.0390	0.0130	0.1763	0.0067	0.0520	0.0215	0.0253	0.0768	0.0007	0.0015	0.0960	0.0570
TriDetect	0.0015	0.1249	0.1253	0.0048	0.0220	0.0000	0.0120	0.1032	0.0030	0.0087	0.0325	0.0110	0.1133	0.0007	0.0001	0.0240	0.0367

Table 15: Comparison on the AIGCDetectBenchmark (Zhong et al. 2023) Dataset in terms of AP Performance. The best result and the second-best result are marked in **bold** and underline, respectively.

Mehod	Grecan	SyleCAN	SyleGAV2	Pocar	Gauc <sub>AN</sub>	StarGAN	BigGAN	Mar	Wukong	Glide	4 g	Noon	MidJourney	50 v.4	SD 11.5	DALLES	£.
CNNSpot	0.4101	0.5390	0.4980	0.5021	0.4636	0.5383	0.4183	0.8075	0.9989	0.9518	0.8329	0.7847	0.8025	0.9999	0.9995	0.9701	0.7198
FreDect	0.4631	0.6684	0.6745	0.7120	0.5859	0.7127	0.8452	0.7140	0.9902	0.7391	0.8651	0.8049	0.7193	0.9971	0.9961	0.8070	0.7684
Fusing	0.4266	0.5229	0.5176	0.4896	0.5019	0.4814	0.4296	0.7288	0.9987	0.9332	0.7774	0.7767	0.6845	0.9999	0.9998	0.9465	0.7009
LGrad	0.4901	0.4992	0.4517	0.5109	0.4777	0.5089	0.5090	0.5226	0.6290	0.6321	0.5079	0.5037	0.5306	0.5937	0.5924	0.5611	0.5325
LNP	0.4154	0.5083	0.4805	0.5012	0.4841	0.4459	0.4621	0.5652	0.9688	0.8129	0.6998	0.6597	0.6395	0.9818	0.9801	0.8051	0.6507
CORE	0.5821	0.6144	0.5383	0.5614	0.5225	0.9743	0.5522	0.8330	0.9975	0.9960	0.7440	0.8272	0.8189	0.9998	0.9997	0.9492	0.7819
SPSL	0.5695	0.5145	0.5038	0.5201	0.5029	0.4950	0.6142	0.5762	0.9924	0.8188	0.8146	0.7588	0.7562	0.9971	0.9957	0.8357	0.7041
UIA-ViT	0.5417	0.6884	0.7113	0.5022	0.4890	0.5831	0.6207	0.6704	0.9949	0.9538	0.9242	0.7873	0.8145	0.9993	0.9988	0.8045	0.7553
DIRE	0.5985	0.6383	0.6571	0.7953	0.4323	0.9937	0.5858	0.8315	0.9968	0.9854	0.8875	0.8362	0.8542	0.9997	0.9993	0.9620	0.8159
UnivFD	0.9641	0.7507	0.7300	0.9301	0.9798	0.8900	0.9704	0.9203	0.9685	0.9915	0.9598	0.9854	0.9275	0.9954	0.9951	0.9562	0.9322
AIDE	0.5267	0.7119	0.6912	0.7424	0.8059	0.6882	0.7557	0.7298	0.9715	0.9149	0.9246	0.8479	0.8706	0.9897	0.9901	0.8723	0.8146
NPR	0.9127	0.9208	0.9486	0.9681	0.5425	0.9998	0.7852	0.9427	0.9874	0.9964	0.9757	0.9593	0.9479	0.9980	0.9973	0.9945	0.9298
Effort	0.9899	0.9510	0.9151	0.9973	0.9997	0.9919	0.9991	0.9088	0.9998	0.9896	0.9979	0.9971	0.9803	1.0000	1.0000	0.9647	0.9801
TriDetect	1.0000	0.9575	0.9020	0.9996	0.9976	1.0000	0.9992	0.9656	0.9999	0.9992	0.9940	0.9992	0.9616	1.0000	1.0000	0.9969	0.9858

Table 16: Comparison on the WildFake (Hong et al. 2025) Dataset in terms of AUC Performance. The best result and the second-best result are marked in **bold** and <u>underline</u>, respectively.

Method	DALL-E	DDIM	DDPM	VQDM	BigGAN	StarGAN	StyleGAN	DF-GAN	GALIP	GigaGAN	Avg
CNNSpot	0.8220	0.5943	0.3375	0.3706	0.9513	0.5003	0.4613	0.5304	0.5143	0.4285	0.5511
FreDect	0.7546	0.7250	0.7385	0.8559	0.9867	0.7985	0.5242	0.8151	0.7686	0.8864	0.7854
Fusing	0.8371	0.7024	0.4468	0.5436	0.9972	0.8057	0.5858	0.5975	0.8207	0.4651	0.6802
LGrad	0.6232	0.5193	0.5236	0.5065	0.5593	0.5172	0.4637	0.5482	0.4033	0.5782	0.5243
LNP	0.8371	0.6025	0.4387	0.6140	0.9401	0.7557	0.6193	0.6148	0.6199	0.5675	0.6610
CORE	0.9213	0.7088	0.5795	0.8723	0.9224	0.7298	0.5879	0.9104	0.7876	0.7192	0.7739
SPSL	0.8470	0.3266	0.2551	0.5248	0.9787	0.4803	0.5476	0.5860	0.4299	0.2803	0.5256
UIA-ViT	0.9045	0.4139	0.3342	0.6346	0.8994	0.5121	0.5507	0.7466	0.6520	0.5660	0.6214
DIRE	0.8880	0.4755	0.4363	0.8621	0.6951	0.5949	0.5216	0.8632	0.8636	0.7628	0.6963
UnivFD	0.5857	0.8008	0.7873	0.7802	0.8711	0.8779	0.6156	0.9597	0.9257	0.8417	0.8046
AIDE	0.6062	0.4235	0.4369	0.6714	0.8322	0.3749	0.5730	0.8317	0.5975	0.3711	0.5718
NPR	0.8056	0.9063	0.7906	0.9339	0.9128	0.8022	0.5161	0.9233	0.7018	0.8276	0.8120
Effort	0.8537	0.8486	0.7197	0.9372	0.9599	0.9023	0.7605	0.9994	0.9343	0.9013	0.8817
TriDetect	0.9189	0.8823	0.7106	0.9787	0.9802	1.0000	0.7245	1.0000	0.9774	0.9981	0.9171

Table 17: Comparison on the WildFake (Hong et al. 2025) Dataset in terms of EER Performance. The best result and the second-best result are marked in **bold** and underline, respectively.

Method	DALL-E	DDIM	DDPM	VQDM	BigGAN	StarGAN	StyleGAN	DF-GAN	GALIP	GigaGAN	Avg
CNNSpot	0.2296	0.4286	0.6301	0.5887	0.1236	0.5006	0.5271	0.4693	0.4796	0.5418	0.4519
FreDect	0.2302	0.2561	0.3288	0.2301	0.0650	0.2778	0.4790	0.2318	0.3013	0.0588	0.2459
Fusing	0.2215	0.3521	0.5538	0.4813	0.0277	0.2662	0.4341	0.4402	0.2556	0.5452	0.3578
LGrad	0.4117	0.4818	0.4721	0.4953	0.4582	0.4896	0.5266	0.4692	0.5731	0.4405	0.4818
LNP	0.2265	0.4292	0.5489	0.4160	0.1371	0.2999	0.4151	0.4153	0.4177	0.4476	0.3753
CORE	0.1409	0.3562	0.4678	0.2096	0.1274	0.3135	0.4390	0.1658	0.2815	0.3399	0.2842
SPSL	0.2116	0.6288	0.6992	0.4826	0.0714	0.5084	0.4611	0.4417	0.5530	0.6577	0.4716
UIA-ViT	0.1731	0.5870	0.6240	0.4113	0.1885	0.5052	0.4705	0.3229	0.3966	0.4452	0.4124
DIRE	0.1939	0.5424	0.5703	0.2235	0.3649	0.4398	0.4888	0.2149	0.2101	0.3060	0.3554
UnivFD	0.4365	0.2179	0.2803	0.2327	0.2162	0.1839	0.4214	0.0445	0.1504	0.2397	0.2423
AIDE	0.4254	0.5607	0.5601	0.3741	0.2535	0.5835	0.4479	0.2408	0.4244	0.5906	0.4461
NPR	0.2507	0.1748	0.2731	0.1376	0.1847	0.2895	0.4903	0.1159	0.3496	0.1906	0.2457
Effort	0.2268	0.2376	0.3516	0.1394	0.1055	0.1859	0.3091	0.0106	0.1505	0.1795	0.1897
TriDetect	0.1508	0.1898	0.3415	0.0691	0.0663	0.0000	0.3391	0.0020	0.0866	0.0167	0.1262

Table 18: Comparison on the WildFake (Hong et al. 2025) Dataset in terms of AP Performance. The best result and the second-best result are marked in **bold** and underline, respectively.

Method	DALL-E	DDIM	DDPM	VQDM	BigGAN	StarGAN	StyleGAN	DF-GAN	GALIP	GigaGAN	Avg
CNNSpot	0.9519	0.8544	0.7365	0.6506	0.9776	0.6501	0.6442	0.6866	0.6657	0.6288	0.7447
FreDect	0.9604	0.9448	0.9048	0.9369	0.9936	0.8776	0.6762	0.9163	0.8374	0.9934	0.9041
Fusing	0.9592	0.9008	0.7733	0.7869	0.9986	0.8655	0.7226	0.7607	0.8838	0.6746	0.8326
LGrad	0.8769	0.8221	0.8005	0.7408	0.7095	0.6816	0.6470	0.7226	0.6294	0.7465	0.7377
LNP	0.9544	0.8586	0.7782	0.8167	0.9679	0.8244	0.7607	0.7595	0.7562	0.7309	0.8207
CORE	0.9801	0.9115	0.8480	0.9419	0.9681	0.8426	0.7368	0.9502	0.8608	0.8340	0.8874
SPSL	0.9591	0.7492	0.6971	0.7532	0.9894	0.6402	0.6913	0.7486	0.6263	0.5519	0.7406
UIA-ViT	0.9730	0.7965	0.7393	0.8210	0.9537	0.6873	0.7224	0.8444	0.7614	0.7281	0.8027
DIRE	0.9694	0.8281	0.7883	0.9326	0.8625	0.7693	0.6945	0.9076	0.8957	0.8312	0.8479
UnivFD	0.8649	0.9606	0.9280	0.9304	0.9345	0.9464	0.7535	0.9937	0.9601	0.9204	0.9192
AIDE	0.8525	0.7664	0.7549	0.7987	0.9202	0.5747	0.6885	0.8673	0.7055	0.5808	0.7510
NPR	0.9452	0.9748	0.9356	0.9745	0.9545	0.8888	0.6931	0.9775	0.8554	0.9435	0.9143
Effort	0.9532	0.9490	0.8936	0.9744	0.9807	0.9493	0.8589	0.9997	0.9652	0.9412	0.9465
TriDetect	0.9794	0.9638	0.8922	0.9924	0.9914	1.0000	0.8385	1.0000	0.9887	0.9991	0.9645

Table 19: Comparison on the DF40 (Yan et al. 2024) Dataset in terms of AUC Performance. The best result and the second-best result are marked in **bold** and underline, respectively.

Method	CollabDiff	MidJourney	DeepFaceLab	StarGAN	StarGAN2	StyleCLIP	WhichisReal	Avg
CNNSpot	0.8890	0.3994	0.5113	0.3954	0.4860	0.7803	0.6265	0.5840
FreDect	0.9764	0.3734	0.5534	0.5091	0.4825	0.8425	0.5550	0.6132
Fusing	0.8969	0.3569	0.6875	0.3920	0.5091	0.6957	0.6581	0.5994
LGrad	0.5063	0.4947	0.4998	0.5078	0.4508	0.4746	0.5185	0.4932
LNP	0.5320	0.3744	0.5476	0.4602	0.5256	0.6324	0.6144	0.5266
CORE	0.8793	0.4534	0.6239	0.5729	0.4340	0.7097	0.3048	0.5683
SPSL	0.7371	0.4621	0.5203	0.5078	0.5399	0.7620	0.6220	0.5930
UIA-ViT	0.9334	0.2430	0.5255	0.3849	0.5068	0.9731	0.4437	0.5729
DIRE	0.9441	0.6177	0.3853	0.3796	0.4355	0.8546	0.4139	0.5758
UnivFD	0.6389	0.8767	0.5013	0.8650	0.7563	0.8841	0.7555	0.7540
NPR	0.0536	0.9541	0.3740	0.4929	0.4542	0.0409	0.8535	0.4605
AIDE	0.7235	0.8004	0.3989	0.7596	0.5697	0.7630	0.6294	0.6635
Effort	0.9991	0.9276	0.5496	0.9859	0.9349	0.9993	0.9122	0.9012
TriDetect	0.9967	0.9147	0.7493	0.9984	0.9450	0.9986	0.9080	0.9301

Table 20: Comparison on the DF40 (Yan et al. 2024) Dataset in terms of EER Performance. The best result and the second-best result are marked in **bold** and underline, respectively.

Method	CollabDiff	MidJourney	DeepFaceLab	StarGAN	StarGAN2	StyleCLIP	WhichisReal	Avg
CNNSpot	0.1920	0.5660	0.4984	0.5766	0.5035	0.2800	0.3980	0.4306
FreDect	0.0850	0.6010	0.4609	0.4950	0.5060	0.2520	0.4700	0.4100
Fusing	0.1800	0.6130	0.3601	0.5806	0.4920	0.3500	0.3750	0.4215
LGrad	0.4960	0.4980	0.4990	0.4990	0.5320	0.5290	0.4870	0.5057
LNP	0.4770	0.5890	0.4628	0.5232	0.4865	0.4120	0.4200	0.4815
CORE	0.1950	0.5500	0.4066	0.4410	0.5360	0.3360	0.6340	0.4427
SPSL	0.3230	0.5300	0.4971	0.4894	0.4715	0.3110	0.4090	0.4330
UIA-ViT	0.1390	0.6950	0.4699	0.5882	0.5035	0.0820	0.5440	0.4317
DIRE	0.1320	0.4210	0.5779	0.5781	0.5415	0.2340	0.5420	0.4324
UnivFD	0.4070	0.2020	0.5288	0.2188	0.3123	0.1990	0.3110	0.3113
NPR	0.8990	0.1150	0.5928	0.5045	0.5370	0.8870	0.2250	0.5372
AIDE	0.3370	0.2760	0.5779	0.3029	0.4444	0.3080	0.4080	0.3792
Effort	0.0110	0.1490	0.4641	0.0590	0.1381	0.0120	0.1770	0.1443
TriDetect	0.0330	0.0720	0.3368	0.0112	0.1326	0.0150	0.1700	0.1229

Table 21: Comparison on the DF40 (Yan et al. 2024) Dataset in terms of AP Performance. The best result and the second-best result are marked in **bold** and <u>underline</u>, respectively.

Method	CollabDiff	MidJourney	DeepFaceLab	StarGAN	StarGAN2	StyleCLIP	WhichisReal	Avg
CNNSpot	0.8976	0.4415	0.6559	0.4226	0.4949	0.9150	0.5899	0.6310
FreDect	0.9798	0.3749	0.6882	0.4961	0.5086	0.9343	0.5533	0.6479
Fusing	0.9057	0.3842	0.7736	0.4139	0.5091	0.8759	0.6037	0.6380
LGrad	0.5249	0.4650	0.6720	0.5044	0.4566	0.7427	0.5309	0.5567
LNP	0.5385	0.3777	0.7004	0.4676	0.5304	0.8215	0.5973	0.5762
CORE	0.8593	0.4463	0.7018	0.5536	0.4407	0.8331	0.3743	0.6013
SPSL	0.7233	0.4231	0.6734	0.4813	0.5292	0.8822	0.5752	0.6125
UIA-ViT	0.9303	0.3268	0.6933	0.4465	0.5091	0.9903	0.4389	0.6193
DIRE	0.9382	0.5679	0.5921	0.4201	0.4487	0.9387	0.4266	0.6189
UnivFD	0.6131	0.8210	0.6957	0.8439	0.7150	0.9539	0.7066	0.7642
NPR	0.3158	0.9549	0.5802	0.4862	0.4690	0.5305	0.8374	0.5963
AIDE	0.6908	0.7314	0.5838	0.7634	0.5311	0.8809	0.5686	0.6786
Effort	0.9992	0.9012	0.6950	0.9851	0.9337	0.9998	0.9042	0.9169
TriDetect	0.9967	0.8635	0.8331	0.9985	0.9461	0.9995	0.9018	0.9342